Geophysical Journal International

Geophys. J. Int. (2011) **186,** 311–330 doi: 10.1111/j.1365-246X.2011.05031.x

Rapid full-wave centroid moment tensor (CMT) inversion in a three-dimensional earth structure model for earthquakes in Southern California

En-Jui Lee,[1] Po Chen,[1] Thomas H. Jordan[2] and Liqiang Wang[3]

[1] *Department of Geology and Geophysics, University of Wyoming, WY* 82071*, USA. E-mail: elee8@uwyo.edu*
[2] *Department of Earth Sciences, University of Southern California, CA, USA*
[3] *Department of Computer Science, University of Wyoming, WY* 82071*, USA*

Accepted 2011 March 31. Received 2011 March 31; in original form 2010 October 2

SUMMARY

A central problem of seismology is the inversion of regional waveform data for models of earthquake sources. In regions such as Southern California, preliminary 3-D earth structure models are already available, and efficient numerical methods have been developed for 3-D anelastic wave-propagation simulations. We describe an automated procedure that utilizes these capabilities to derive centroid moment tensors (CMTs). The procedure relies on the use of receiver-side Green's tensors (RGTs), which comprise the spatial-temporal displacements produced by the three orthogonal unit impulsive point forces acting at the receivers. We have constructed a RGT database for 219 broad-band stations in Southern California using a tomographically improved version of the 3-D SCEC Community Velocity Model Version 4.0 (CVM4) and a staggered-grid finite-difference code. Finite-difference synthetic seismograms for any earthquake in our modelling volume can be simply calculated by extracting a small, source-centred volume from the RGT database and applying the reciprocity principle. The partial derivatives needed for the CMT inversion can be generated in the same way. We have developed an automated algorithm that combines a grid-search for suitable focal mechanisms and hypocentre locations with a Gauss–Newton optimization that further refines the grid-search results. Using this algorithm, we have determined CMT solutions for 165 small to medium-sized earthquakes in Southern California. Preliminary comparison with the CMT solutions provided by the Southern California Seismic Network (SCSN) shows that our solutions generally provide better fit to the observed waveforms. When applied to a large number of earthquakes, our algorithm may provide a more robust CMT catalogue for earthquakes in Southern California.

Key words: Probability distributions; Earthquake ground motions; Earthquake source observations; Computational seismology; Wave propagation; Early warning.

1 INTRODUCTION

Accurate and rapid seismic source parameter inversions are important for seismic hazard analysis in earthquake-prone areas such as Southern California. The Southern California Seismic Network (SCSN) routinely determines the focal mechanisms from first-motion polarities for earthquakes with local magnitude as low as 2.0–2.5 (Hauksson 2000). With the advancement of digital broad-band instrumentation, complete Centroid Moment Tensor (CMT; Dziewonski *et al.* 1981) solutions can be automatically recovered from regional broad-band waveform data for earthquakes with local magnitude larger than 3.0 (Dreger & Helmberger 1991; Zhao & Helmberger 1994; Thio & Kanamori 1995; Pasyanos *et al.* 1996; Zhu & Helmberger 1996; Liu *et al.* 2004; Clinton *et al.* 2006).

In the waveform inversion approach, an optimal CMT solution is found by minimizing a certain measure of the waveform misfit between observed and model-predicted (synthetic) seismograms either in time domain (e.g. Zhao & Helmberger 1994; Zhu & Helmberger 1996) or in frequency domain (e.g. Romanowicz *et al.* 1993; Thio & Kanamori 1995). To reduce computational cost, synthetic seismograms as well as their partial derivatives with respect to CMT parameters are often computed in simple 1-D earth structure models using semi-analytic methods (e.g. Zhao & Helmberger 1994; Dreger 2003). Multiple 1-D structure models can be adopted to account for gross lateral variations in crustal structure. And phases that are relatively insensitive to crustal heterogeneities, such as long-period surface waves and P_{nl}, the combination of P_{n} and PL (Helmberger & Engen 1980), can be used in the inversion to alleviate the dependence on structure models. Difficulties may arise when attempting inversions for smaller earthquakes, as the signal-to-noise ratio (SNR) at long periods may become too low for smaller earthquakes ($M_w \leq 3.7$). For inversions at shorter periods, small-scale lateral variations in crustal structure can become important and to further accommodate those small-scale structural variations, simple time shifts between portions of observed and synthetic seismograms are allowed while minimizing the waveform misfit (e.g. Zhao & Helmberger 1994; Zhu & Helmberger 1996).

Recent advances in parallel computing technology and numerical methods (Olsen 1994; Graves 1996; Akçelik *et al*. 2003; Olsen *et al*. 2003; Komatitsch *et al.* 2004) have made large-scale 3-D numerical simulations of seismic wavefields much more affordable, and they open up the possibility of using highly accurate synthetic Green's functions computed in 3-D earth structure models in source parameter inversions. Synthetic Green's functions computed from a good 3-D earth structure model can account for complex wave phenomena and reduce phase differences with observed waveforms. Ramos-Martínez & McMechan (2001) developed a full-waveform focal mechanism inversion algorithm that uses synthetic Green's functions computed for a 3-D heterogeneous viscoelastic anisotropic structure model using a staggered-grid finite-difference method and applied it to two aftershocks of the 1994 M_w 6.7 Northridge earthquake. They found that incorporation of realistic 3-D structure reduced the residual errors of the waveform fitting by more than 50 per cent compared to those for a 1-D layered model. In their algorithm, source locations are not inverted. Liu *et al.* (2004) developed a full-waveform CMT inversion technique using synthetic Green's functions computed in the 3-D Harvard crustal structure model for Southern California (Süss & Shaw 2003) based on the spectral-element method (Komatitsch *et al.* 2004). The partial derivatives of the synthetic waveforms with respect to the six moment tensor components and the source location were evaluated numerically through differencing. Up to 10 wave-propagation simulations were needed to calculate all partial derivatives. When the initial location is far from the true location, non-linear, iterative optimization algorithms can be adopted but the computational cost can become quite high for obtaining a robust solution in a short period of time after the earthquake. A similar approach has been recently adapted to continental scale in Hingee *et al.* (2010) using a 3-D structure model for the Australasian region obtained through full-wave adjoint tomography (Fichtner *et al.* 2009; Fichtner *et al.* 2010). A number of sensitivity tests show that the 3-D model is superior to a well-calibrated 1-D model in obtaining accurate CMT solutions.

As numerical simulations of seismic wavefields in 3-D structure models are still computationally intensive, if we perform forward simulations for every potential source model, it is very impractical for rapid or (near) real-time applications. A more practical approach for rapid CMT inversions in a 3-D earth structure model is to use the reciprocity principle (Aki & Richards 2002; Okamoto 1994a,b; Okamoto 2002). Zhao *et al.* (2006) introduced the use of receiver Green's tensors (RGTs) for source parameter inversions in 3-D earth structure models by taking advantage of the reciprocity principle. The RGTs are the strain fields, as functions of both space and time, generated by three orthogonal unit impulsive point forces acting at the receiver locations. By applying the reciprocity principle, it can be shown that the RGTs provide exact partial derivatives of the waveforms at the receiver locations with respect to the moment tensor at any point in the modelling volume. The RGTs can be calculated with high accuracy in a 3-D earth structure model using numerical methods, such as finite-difference, finite-element and spectral-element methods, and stored in a database. Since the synthetic seismograms and their partial derivatives can be retrieved from the database very rapidly, the RGT-based approach is better suited for (near) real-time source parameter inversions. The disadvantage of this approach is that since the RGT database has to be constantly on-line for rapid access, the disk storage cost could be quite high. The computational and storage costs for CMT inversions using RGTs calculated in a 3-D structure model for the Los Angeles basin region based on the finite-difference method were summarized in Chen *et al.* (2007). Traditional high-performance computing platforms such as distributed-memory computer clusters are usually shared by multiple users and suffer from long delays in acquiring computational resources. The emerging cloud computing platform allows users to acquire and release resources on-demand with very low scheduling overheads and may provide a much more cost-effective alternative for RGT-based (near) real-time synthetic seismogram calculations and source parameter inversions (Subramanian *et al.* 2010).

In Zhao *et al.* (2006), an iterative optimization approach based on the Gauss–Newton algorithm was adopted and to initiate the optimization process a reference source model is needed. In that study, the reference source location was obtained from the relocated hypocentre catalogue SHLK (Shearer *et al.* 2005) and it was not perturbed during the optimization. The reference focal mechanism was estimated from first-motion polarity data using the HASH algorithm (Hardebeck & Shearer 2002), which carries out a grid search for suitable dip, rake and strike angles that best fit the polarities of the first motions. In this paper, we extend the RGT-based CMT inversion algorithm in Zhao *et al.* (2006) to include a grid search in the vicinity of the reference locations for suitable focal mechanisms and source locations that minimize different measures of waveform misfit. The source models obtained from the grid-search step are then used as the initial solutions in the subsequent iterative optimization process based on the Gauss–Newton algorithm. The grid-search step is computationally efficient as it involves retrieving from the pre-computed RGT database a small volume centred at the reference source location and no additional 3-D wave-propagation simulations are needed. We have applied our CMT inversion algorithm to 165 earthquakes in Southern California. In general, our CMT solutions are consistent with solutions obtained using other methods and usually provide better fit to the observed waveforms. Our CMT inversion algorithm does not require manual intervention, when combined with real-time access to telemetered, digital data streams from the seismic network, our algorithm has the potential to provide improved moment tensor estimates in (near) real-time.

2 METHODOLOGY

In general, the moment tensor **M** has six independent elements. For a purely deviatoric source, we require the trace of **M** to be zero. For a purely double couple source, we further require the determinant of **M** to be zero. Following Kikuchi & Kanamori (1991), we represent a general moment tensor $\mathbf{M}$ as a linear combination of six elementary basis moment tensors $\mathbf{M}_m$,

$$\mathbf{M} = \sum_{m=1}^{6} a_m \mathbf{M}_m, \tag{1}$$

where a_m is the coefficient for the basis moment tensor $\mathbf{M}_m$ and the six basis moment tensors are given by

$$\mathbf{M}_1 = \begin{bmatrix} 0 & 1 & 0 \\ 1 & 0 & 0 \\ 0 & 0 & 0 \end{bmatrix}; \quad \mathbf{M}_2 = \begin{bmatrix} -1 & 0 & 0 \\ 0 & 1 & 0 \\ 0 & 0 & 0 \end{bmatrix}; \quad \mathbf{M}_3 = \begin{bmatrix} 0 & 0 & -1 \\ 0 & 0 & 0 \\ -1 & 0 & 0 \end{bmatrix};$$

$$\mathbf{M}_4 = \begin{bmatrix} 0 & 0 & 0 \\ 0 & 0 & -1 \\ 0 & -1 & 0 \end{bmatrix}; \quad \mathbf{M}_5 = \begin{bmatrix} 0 & 0 & 0 \\ 0 & -1 & 0 \\ 0 & 0 & 1 \end{bmatrix}; \quad \mathbf{M}_6 = \begin{bmatrix} 1 & 0 & 0 \\ 0 & 1 & 0 \\ 0 & 0 & 1 \end{bmatrix}. \tag{2}$$

We note that different from Kikuchi & Kanamori (1991) the coordinate system (x, y, z) for M_{ij} adopted in this study corresponds to (east, north, up) and the resulting basis moment tensors in eq. (2) are different from those in Kikuchi & Kanamori (1991).

An important advantage for decomposing an arbitrary moment tensor into a linear combination of the six basis moment tensors is that specific solutions, such as pure-deviatoric moment tensors (represented using $\mathbf{M}_1$–$\mathbf{M}_5$), general double couple solutions (represented using $\mathbf{M}_1$–$\mathbf{M}_5$ with zero determinant), double couple solutions with a vertical nodal plane (represented using $\mathbf{M}_1$–$\mathbf{M}_4$ with zero determinant) and pure strike-slip solutions (represented using $\mathbf{M}_1$ and $\mathbf{M}_2$) can be obtained from subgroups of the six basis moment tensors (Kikuchi & Kanamori 1991) and certain constraints can be incorporated into the inversion through selectively inverting for a subgroup of the six coefficients a_m. The synthetic seismogram at receiver location $\mathbf{r}_\mathrm{R}$ due to a source at $\mathbf{r}_\mathrm{S}$ with a general moment tensor $\mathbf{M}$ can thus be expressed as a linear combination of the synthetics for the six basis moment tensors

$$u_k(\mathbf{r}_\mathrm{R}, t; \mathbf{r}_\mathrm{S}) = \sum_{m=1}^{6} a_m g_{km}(\mathbf{r}_\mathrm{R}, t; \mathbf{r}_\mathrm{S}), \tag{3}$$

where $g_{km}(\mathbf{r}_\mathrm{R}, t; \mathbf{r}_\mathrm{S})$ is the kth component synthetic seismogram due to basis moment tensor $\mathbf{M}_m$ and is computed from the RGT by applying the reciprocity principle.

2.1 Receiver Green's tensors (RGTs)

Following Zhao *et al.* (2006), the displacement field from a point source located at $\mathbf{r}'$ with moment tensor M_{ij} can be expressed as (e.g. Aki & Richards 2002, equation 3.23)

$$u_k(\mathbf{r}, t; \mathbf{r}') = M_{ij} \partial'_j G_{ki}(\mathbf{r}, t; \mathbf{r}'), \tag{4}$$

where ∂'_j denotes the source-coordinate gradient with respect to $\mathbf{r}'$ and the Green's tensor $G_{ki}(\mathbf{r}, t; \mathbf{r}')$ relates a unit impulsive force acting at location $\mathbf{r}'$ in direction $\hat{\mathbf{e}}_i$ to the displacement response at location $\mathbf{r}$ in direction $\hat{\mathbf{e}}_k$. Taking into account the symmetry of the moment tensor, we also have

$$u_k(\mathbf{r}, t; \mathbf{r}') = \frac{1}{2}\left[\partial'_j G_{ki}(\mathbf{r}, t; \mathbf{r}') + \partial'_i G_{kj}(\mathbf{r}, t; \mathbf{r}')\right] M_{ij}. \tag{5}$$

Applying reciprocity of the Green's tensor

$$G_{ki}(\mathbf{r}, t; \mathbf{r}') = G_{ik}(\mathbf{r}', t; \mathbf{r}), \tag{6}$$

eq. (5) can be written as

$$u_k(\mathbf{r}, t; \mathbf{r}') = \frac{1}{2}\left[\partial'_j G_{ik}(\mathbf{r}', t; \mathbf{r}) + \partial'_i G_{jk}(\mathbf{r}', t; \mathbf{r})\right] M_{ij}. \tag{7}$$

For a given receiver location $\mathbf{r} = \mathbf{r}_\mathrm{R}$, the RGT is a third-order tensor defined as the spatial-temporal strain field

$$H_{jik}(\mathbf{r}', t; \mathbf{r}_\mathrm{R}) = \frac{1}{2}\left[\partial'_j G_{ik}(\mathbf{r}', t; \mathbf{r}_\mathrm{R}) + \partial'_i G_{jk}(\mathbf{r}', t; \mathbf{r}_\mathrm{R})\right]. \tag{8}$$

Using this definition, the displacement recorded at receiver location $\mathbf{r}_\mathrm{R}$ due to a source at $\mathbf{r}_\mathrm{S}$ with moment tensor $\mathbf{M}$ can be expressed as

$$u_k(\mathbf{r}_\mathrm{R}, t; \mathbf{r}_\mathrm{S}) = M_{ij} H_{jik}(\mathbf{r}_\mathrm{S}, t; \mathbf{r}_\mathrm{R}) \text{ or } \mathbf{u}(\mathbf{r}_\mathrm{R}, t; \mathbf{r}_\mathrm{S}) = \mathbf{M} : \mathbf{H}(\mathbf{r}_\mathrm{S}, t; \mathbf{r}_\mathrm{R}), \tag{9}$$

and the synthetic seismogram due to a source at $\mathbf{r}_\mathrm{S}$ with the basis moment tensor $\mathbf{M}_m$ can be expressed as

$$\mathbf{g}_m(\mathbf{r}_\mathrm{R}, t; \mathbf{r}_\mathrm{S}) = \mathbf{M}_m : \mathbf{H}(\mathbf{r}_\mathrm{S}, t; \mathbf{r}_\mathrm{R}). \tag{10}$$

Most of the numerical algorithms for solving the seismic wave equation, such as finite-difference, finite-element and spectral-element methods, explicitly use the spatial gradients of the displacement (or velocity) and the stress (or stress rate) in their calculations. For a given receiver, the RGT can therefore be computed through three wave-propagation simulations with a unit impulsive force acting at the receiver location $\mathbf{r}_\mathrm{R}$ and pointing in the direction $\hat{\mathbf{e}}_k$ ($k = 1, 2, 3$) in each simulation and store the strain fields at all spatial grid points $\mathbf{r}'$ and all time sample t. The synthetic seismogram at the receiver due to any point source located within the modelling domain can be obtained by retrieving the strain Green's tensor at the source location from the RGT volume and then applying eq. (9).

2.2 Grid search based on Bayesian inference

For each earthquake, we consider a random vector H composed of six source parameters: the longitude, latitude and depth of the centroid location $\mathbf{r}_S$, and the strike, dip and rake of the focal mechanism. We assume a uniform prior probability $P_0(H)$ over a sample space Ω_0, which is defined as a subgrid in our modelling volume centred around the initial hypocentre location provided by the seismic network with grid spacing in three orthogonal directions given by a vector $\mathbf{h}_0$ and a focal mechanism space with the ranges given by $0^\circ \le$ strike $\le 360^\circ$, $0^\circ \le$ dip $\le 90^\circ$ and $-90^\circ \le$ rake $\le 90^\circ$ and with angular intervals in strike, dip and rake specified by a vector θ_0. The strike, dip and rake values can be converted into the Cartesian components of the moment tensor $\mathbf{M}$ (Aki & Richards 2002), which can be subsequently converted into the six coefficients a_m through a simple algebraic manipulation. Synthetic seismograms for each source parameter vector in the sample space can then be computed using the RGT database by applying eqs (3) and (10) above.

We apply Bayesian inference in three steps sequentially. In the first step, the likelihood function is defined in terms of waveform similarity between synthetic and observed seismograms. We quantify waveform similarity using a normalized correlation coefficient (NCC) defined as

$$\mathrm{NCC}_n = \max_{\Delta t} \left[\int_{t_n^0}^{t_n^1} \bar{s}_n(t) s_n(t-\Delta t)dt \Bigg/ \sqrt{\int_{t_n^0}^{t_n^1} \bar{s}_n^2(t)dt \int_{t_n^0}^{t_n^1} s_n^2(t-\Delta t)dt} \right], \tag{11}$$

where n is the observation index, $\bar{s}_n(t)$ and $s_n(t)$ are the filtered observed seismogram and the corresponding synthetic seismogram, $[t_n^0, t_n^1]$ is the time window for selecting a certain phase on the seismograms for cross-correlation. We allow a certain time-shift Δt between the observed and synthetic waveforms. To prevent possible cycle-skipping errors, we restrict $|\Delta t|$ to be less than half of the shortest period. We assume a truncated exponential distribution for the conditional probability

$$P(\mathrm{NCC}_n|H_q) = \frac{\lambda_n \exp[-\lambda_n(1-\mathrm{NCC}_n)]}{1-\exp(-2\lambda_n)}, \quad -1 < \mathrm{NCC}_n \le 1, \quad H_q \in \Omega_0, \tag{12}$$

where λ_n is the decay rate. Assuming the NCC observations are independent, the likelihood function can be expressed as

$$L_0\left(H \middle| \bigcap_{n=1}^{N} \mathrm{NCC}_n\right) = \exp\left[-\sum_{n=1}^{N} \lambda_n (1-\mathrm{NCC}_n)\right] \prod_{n=1}^{N} \left\{\lambda_n [1-\exp(-2\lambda_n)]^{-1}\right\}, \tag{13}$$

where N is the total number of NCC observations. The posterior probability for the first step can then be expressed as

$$P_0\left(H \middle| \bigcap_{n=1}^{N} \mathrm{NCC}_n\right) = \frac{P_0(H)\exp\left[-\sum_{n=1}^{N} \lambda_n (1-\mathrm{NCC}_n)\right] \prod_{n=1}^{N} \left\{\lambda_n [1-\exp(-2\lambda_n)]^{-1}\right\}}{P_0\left(\bigcap_{n=1}^{N} \mathrm{NCC}_n\right)}, \tag{14}$$

where

$$P_0\left(\bigcap_{n=1}^{N} \mathrm{NCC}_n\right) = \sum_q P\left(\bigcap_{n=1}^{N} \mathrm{NCC}_n|H_q\right) P_0(H_q). \tag{15}$$

We note that the λ_n in front of $(1-\mathrm{NCC}_n)$ in eq. (14) can be used as a weighting factor for various purposes, such as to account for different SNRs in observed seismograms and to avoid the solution to be dominated by a cluster of closely spaced seismic stations.

The probability for individual measurements

$$P_0(\mathrm{NCC}_n) \propto \sum_q P(\mathrm{NCC}_n|H_q)P_0(H_q) \tag{16}$$

can be used for rejecting problematic observations. In practice, we only accept observations with

$$P_0(\mathrm{NCC}_n) \ge Q_0. \tag{17}$$

A very low $P_0(\mathrm{NCC}_n)$ indicates that the nth observed waveform cannot be fit well by any solutions in our sample space. This may be due to instrumentation problems or unusually high noise levels in the observed waveform data.

In the second step, the posterior probability from the first step, eq. (14), is used as the prior probability

$$P_1(H) = P_0\left(H \middle| \bigcap_{n=1}^{N} \mathrm{NCC}_n\right), \tag{18}$$

and the sample space for the second step, Ω_1, consists of source parameter vectors H that satisfy

$$P_1(H) \ge \bar{P}_1, \tag{19}$$

where $\bar{P}_1$ is a threshold used to reject source parameters with low probabilities. The sampling intervals for centroid location and focal mechanism are reduced to $\mathbf{h}_1$ and θ_1, respectively and synthetic seismograms for the new sample space Ω_1 are computed using eqs (3) and (10). The likelihood function for the second step is defined in terms of the time-shift ΔT_n that maximizes the NCC observation as defined in eq. (11). We assume an exponential distribution for the conditional probability

$$P(\Delta T_n|H_q) = \mu_n \exp(-\mu_n|\Delta T_n - \Delta T_M|), \quad H_q \in \Omega_1, \tag{20}$$

where μ_n is the decay rate and ΔT_M is the median of all ΔT_n observations. Assuming the ΔT_n observations are independent, the likelihood function for the second step can be expressed as

$$L_1\left(H\left|\bigcap_{n=1}^{N}\Delta T_n\right.\right) = \exp\left(-\sum_{n=1}^{N}\mu_n\,|\Delta T_n - \Delta T_M|\right)\prod_{n=1}^{N}\mu_n \tag{21}$$

and the posterior probability for the second step can be expressed as

$$P_1\left(H\left|\bigcap_{n=1}^{N}\Delta T_n\right.\right) = P_1(H)\exp\left(-\sum_{n=1}^{N}\mu_n\,|\Delta T_n - \Delta T_M|\right)\prod_{n=1}^{N}\mu_n \Bigg/ P_1\left(\bigcap_{n=1}^{N}\Delta T_n\right), \tag{22}$$

where

$$P_1\left(\bigcap_{n=1}^{N}\Delta T_n\right) = \sum_q P\left(\bigcap_{n=1}^{N}\Delta T_n|H_q\right)P_1(H_q). \tag{23}$$

We note that like λ_n, the decay rate μ_n in eq. (22) can also be used as a weighting factor. The probability for individual observation

$$P_1(\Delta T_n) \propto \sum_q P\left(\Delta T_n|H_q\right)P_1(H_q) \tag{24}$$

can be used for controlling observation quality, and we only accept observations with

$$P_1(\Delta T_n) \geq Q_1. \tag{25}$$

In the third step, the posterior probability from the second step, eq. (22), is used as the prior probability

$$P_2(H) = P_1\left(H\left|\bigcap_{n=1}^{N}\Delta T_n\right.\right). \tag{26}$$

The sample space for the third step, Ω_2, consists of source parameter vectors H that satisfy

$$P_2(H) \geq \bar{P}_2, \tag{27}$$

where $\bar{P}_2$ is our second threshold for rejecting source parameters with low probabilities. The sampling intervals for centroid location and focal mechanism are further reduced to $\mathbf{h}_2$ and θ_2, respectively and synthetic seismograms for the new sample space Ω_2 are computed. The likelihood function in the third step is defined in terms of the amplitude anomaly (Ritsema *et al.* 2002)

$$A_n = \int_{t_n^0}^{t_n^1}\bar{s}_n(t)s_n(t-\Delta T_n)dt \Bigg/ \int_{t_n^0}^{t_n^1}s_n(t)s_n(t-\Delta T_n)dt, \tag{28}$$

where ΔT_n is the time-shift that maximizes the NCC observation. We assume an exponential distribution for the conditional probability

$$P(A_n|H_q) = \gamma_n \exp\left(-\gamma_n\,|\ln(A_n) - \ln(A_M)|\right), \quad H_q \in \Omega_2, \tag{29}$$

where A_M is the median of all A_n observations. Assuming the amplitude anomaly observations are independent, the likelihood function can be expressed as

$$L_2\left(H\left|\bigcap_{n=1}^{N}A_n\right.\right) = \exp\left(-\sum_{n=1}^{N}\gamma_n\,|\ln(A_n) - \ln(A_M)|\right)\prod_{n=1}^{N}\gamma_n, \tag{30}$$

and the posterior probability for the third step can be expressed as

$$P_2\left(H\left|\bigcap_{n=1}^{N}A_n\right.\right) = P_2(H)\exp\left(-\sum_{n=1}^{N}\gamma_n\,|\ln(A_n) - \ln(A_M)|\right)\prod_{n=1}^{N}\gamma_n \Bigg/ P_2\left(\bigcap_{n=1}^{N}A_n\right), \tag{31}$$

where

$$P_2\left(\bigcap_{n=1}^{N}A_n\right) = \sum_q P\left(\bigcap_{n=1}^{N}A_n|H_q\right)P_2(H_q). \tag{32}$$

The probability for individual observations

$$P_2(A_n) \propto \sum_q P\left(A_n|H_q\right)P_2(H_q) \tag{33}$$

can be used to reject problematic observations, and we require

$$P_2(A_n) \geq Q_2. \tag{34}$$

After the third step is completed, the source parameter vector H_M that maximizes the posterior probability in eq. (31) is selected as our optimal estimate. The centroid time is estimated as

$$T_\mathrm{S} = \Delta T_M, \tag{35}$$

where ΔT_M is the median of all time-shift observations ΔT_n measured for the optimal source parameter vector H_M. The scalar seismic moment is estimated as

$$M_0 = A_M, \tag{36}$$

where A_M is the median of all A_n observations measured for the optimal source parameter vector H_M.

An important advantage of the Bayesian approach is that, instead of a single best solution, the complete posterior probability density on the sample space is obtained, which allows formal estimation of the uncertainties associated with the derived source parameters. In Fig. 4, examples of the marginal probabilities for some of the source parameters are shown for the 2002 September 3 Yorba Linda earthquake.

2.3 Gauss–Newton optimization

The optimal source parameter vector H_M together with the estimates of centoid time T_S and scalar seismic moment M_0 are used as the initial solution in an iterative Gauss–Newton optimization procedure to further refine our estimates of the centroid location, centroid time and the coefficients for the six basis moment tensors a_m.

Following Zhao *et al.* (2006), we quantify the waveform misfit between the observed and synthetic waveforms using the generalized seismological data functionals (GSDF; Gee & Jordan 1992). In the frequency domain, we can map the synthetic waveform $u_i(\mathbf{r}_\mathrm{R}, \omega)$ into the observed waveform $\bar{u}_i(\mathbf{r}_\mathrm{R}, \omega)$ using two frequency-dependent, time-like quantities $\delta\tau_\mathrm{p}(\mathbf{r}_\mathrm{R}, \omega)$ and $\delta\tau_\mathrm{q}(\mathbf{r}_\mathrm{R}, \omega)$

$$\bar{u}_i^s(\mathbf{r}_\mathrm{R}, \omega) = u_i^s(\mathbf{r}_\mathrm{R}, \omega) \exp\left\{ i\omega \left[\delta\tau_\mathrm{p}(\mathbf{r}_\mathrm{R}, \omega) + i\delta\tau_\mathrm{q}(\mathbf{r}_\mathrm{R}, \omega) \right] \right\}, \tag{37}$$

and in GSDF analysis, we estimate $\delta\tau_\mathrm{p,q}(\mathbf{r}_\mathrm{R}, \omega)$ by measuring frequency-dependent phase-delay time $\delta t_\mathrm{p}(\mathbf{r}_\mathrm{R}, \omega_n)$ and amplitude-reduction time $\delta t_\mathrm{q}(\mathbf{r}_\mathrm{R}, \omega_n)$ at a set of discrete frequencies of interest ω_n. The GSDF measurements can be expressed in terms of waveform perturbation using the seismogram perturbation kernel (Chen *et al.* 2007, 2010)

$$\delta t_\mathrm{x}(\mathbf{r}_\mathrm{R}, \omega_n) = \int dt\, J_\mathrm{x}(t, \mathbf{r}_\mathrm{R}, \omega_n)\, \delta u_k(\mathbf{r}_\mathrm{R}, t - t_\mathrm{S}; \mathbf{r}_\mathrm{S}), \quad (\mathrm{x} = \mathrm{p}, \mathrm{q}). \tag{38}$$

Explicit expressions of the perturbation kernels J_x for GSDF measurements are presented in Chen *et al.* (2010). The waveform perturbation can be expressed in terms of perturbations of centroid time t_S, centroid location $\mathbf{r}_\mathrm{S}$ and a_m as

$$\delta u_k(\mathbf{r}_\mathrm{R}, t - t_\mathrm{S}; \mathbf{r}_\mathrm{S}) = -\dot{u}_k(\mathbf{r}_\mathrm{R}, t - t_\mathrm{S}; \mathbf{r}_\mathrm{S})\delta t_\mathrm{S} + \nabla_\mathrm{S} u_k(\mathbf{r}_\mathrm{R}, t - t_\mathrm{S}; \mathbf{r}_\mathrm{S}) \cdot \delta\mathbf{r}_\mathrm{S} + \sum_{m=1}^{6} g_{km}(\mathbf{r}_\mathrm{R}, t - t_\mathrm{S}; \mathbf{r}_\mathrm{S})\delta a_m, \tag{39}$$

where ∇_S is the gradient with respect to source coordinates $\mathbf{r}_\mathrm{S}$, $\dot{u}_k(\mathbf{r}_\mathrm{R}, t - t_\mathrm{S}; \mathbf{r}_\mathrm{S})$ and $\nabla_\mathrm{S} u_k(\mathbf{r}_\mathrm{R}, t - t_\mathrm{S}; \mathbf{r}_\mathrm{S})$ are the synthetic velocity and strain field at the reference time t_S and reference location $\mathbf{r}_\mathrm{S}$. The synthetic velocity and strain Green's tensor fields are explicitly calculated and stored in our RGT-based algorithm (Zhao *et al.* 2006), therefore the partial derivatives of the waveform with respect to source parameters t_S, $\mathbf{r}_\mathrm{S}$ and a_m can be readily calculated from our RGT database. The partial derivatives of the GSDF measurements with respect to the source parameters can be obtained by combining eq. (38) and (39) through the chain rule.

3 THREE-DIMENSIONAL EARTH STRUCTURE MODEL

In this study, we have computed and stored the RGTs for 219 Southern California Seismic Network (SCSN) stations in the region shown in Fig. 1 using a tomographically updated version of the 3-D earth structure model, Southern California Earthquake Center (SCEC) Community Velocity Model Version 4.0 (CVM4) (Magistrale *et al.* 2000; Kohler *et al.* 2003), and a fourth-order staggered-grid finite-difference code (Olsen 1994).

The seismic velocity model SCEC CVM4 is composed of detailed, rule-based representation of major basins embedded in a 3-D regional crust model. The background seismic velocities were interpolated from the 3-D crustal model constructed from regional traveltime tomography (Hauksson 2000). Within the basins the *P* velocity was determined from the age and depth of sediments using empirical relations and the *S* velocity was then scaled from *P* velocity with a given Poisson's ratio. The Moho in CVM4 is represented with a variable-depth surface, which was determined using the receiver function technique (Zhu & Kanamori 2000).

Using the 3-D SCEC CVM4 as our starting model, we have carried out two iterations of full 3-D tomography using the scattering-integral method (Zhao *et al.* 2005; Chen *et al.* 2007). This updated 3-D seismic structure model is named CVM4SI2. To obtain CVM4SI2, we inverted about 7000 cross-correlation traveltime measurements made on body- and surface-waves generated by local earthquakes and surface-waves extracted from ambient-noise Green's functions (Ma *et al.* 2008). Compared with CVM4, the variance-reduction in cross-correlation traveltime measurements for CVM4SI2 is about 40 per cent. The updated model CVM4SI2 provides substantially better fit to observed waveforms than the starting model CVM4 for frequencies up to 0.2 Hz. Examples of improvements in waveform fitting for some source-station (for earthquake waveform data) and station–station (for ambient-noise Green's function data) paths are shown in Fig. 2. Compared with CVM4, CVM4SI2

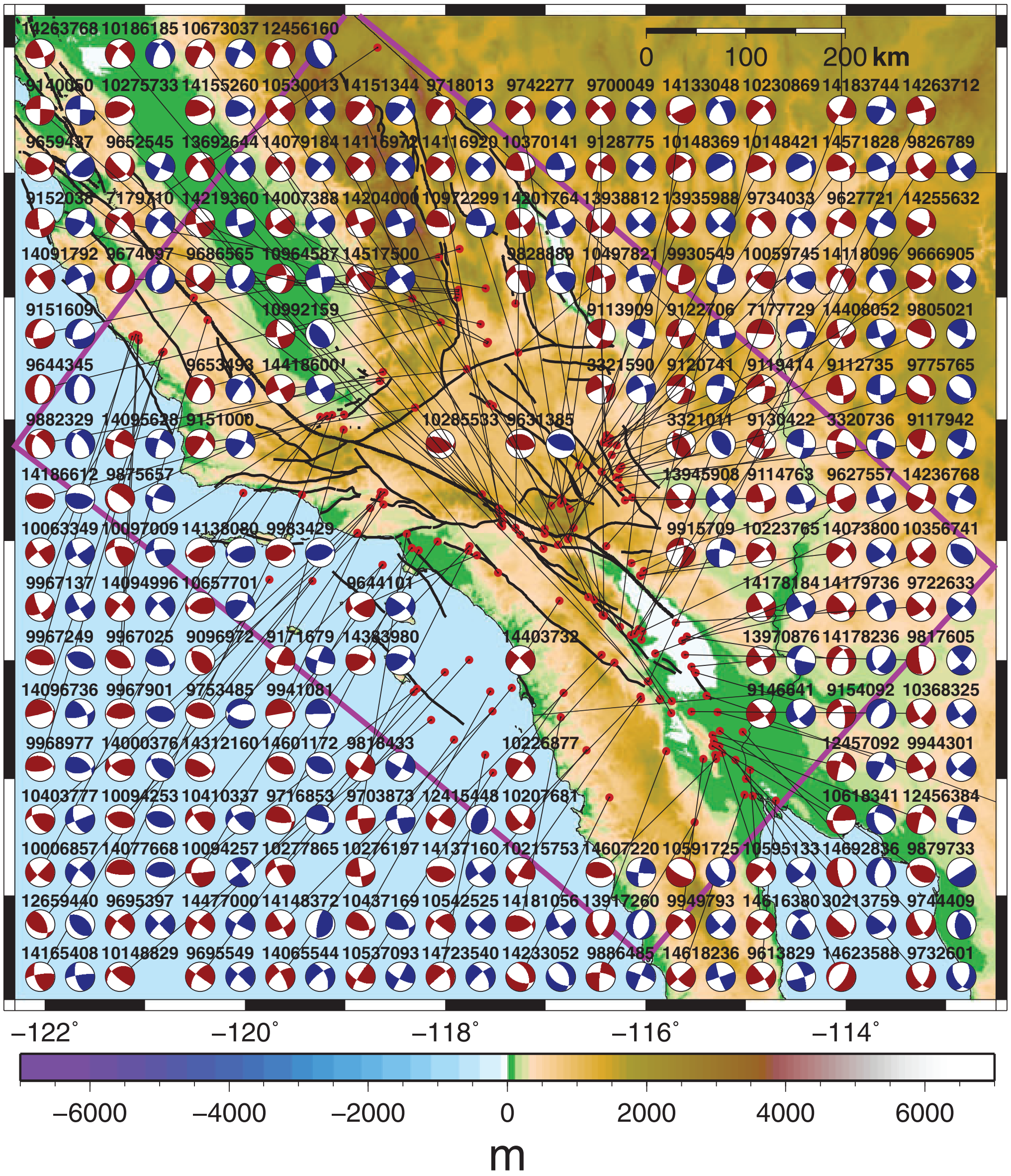

Figure 1. The focal mechanisms for the 165 earthquakes analysed in this study. Red beachballs, focal mechanisms obtained using our CMT inversion algorithm; blue beachballs, SCSN focal mechanisms. SCSN event numbers for those earthquakes are listed above the beachballs. Red dots indicate the epicentres of those earthquakes. The purple box indicates our study area. Major faults in this area are plotted in black solid lines. The background colour shows topography.

has lower velocities in the Mojave block and high velocities in the Los Angeles Basin and the Ventura Basin. Currently, CVM4SI2 is still being refined through full –3-D, full-wave tomography using waveform data from local earthquakes and ambient-noise Green's functions. The details of our tomographic inversion for Southern California will be documented in a separate paper. At the current stage, we feel that CVM4SI2 has sufficient accuracy to provide improved CMT estimates for local earthquakes.

The finite-difference wave-propagation simulations needed for constructing the RGT database were carried out in CVM4SI2. The 768-km long, 496-km wide and 50-km deep modelling volume (Fig. 1) was discretized into a uniform mesh with 500 m grid-spacing and 152 million grid points, which is sufficient for achieving accurate simulation results for frequencies up to 0.2 Hz. Synthetic seismograms for source locations right on our grid points were extracted directly from our RGT database by applying eqs (3) and (10). Synthetics for source locations off our grid points were generated from the strain fields at the surrounding grid points using a trilinear interpolation algorithm. Our numerical experiments have shown that this interpolation algorithm provides synthetics with sufficient accuracy for frequencies up to 0.2 Hz.

To demonstrate the importance of the 3-D earth structure model in improving the accuracy of our synthetic seismograms compared with a well-calibrated laterally homogeneous 1-D velocity model, we use the 2008 July 29 M_w 5.4 Chino Hills earthquake as an example. This earthquake is located close to the centre of our modelling region and at a depth of about 14 km (Fig. 3). This earthquake was well

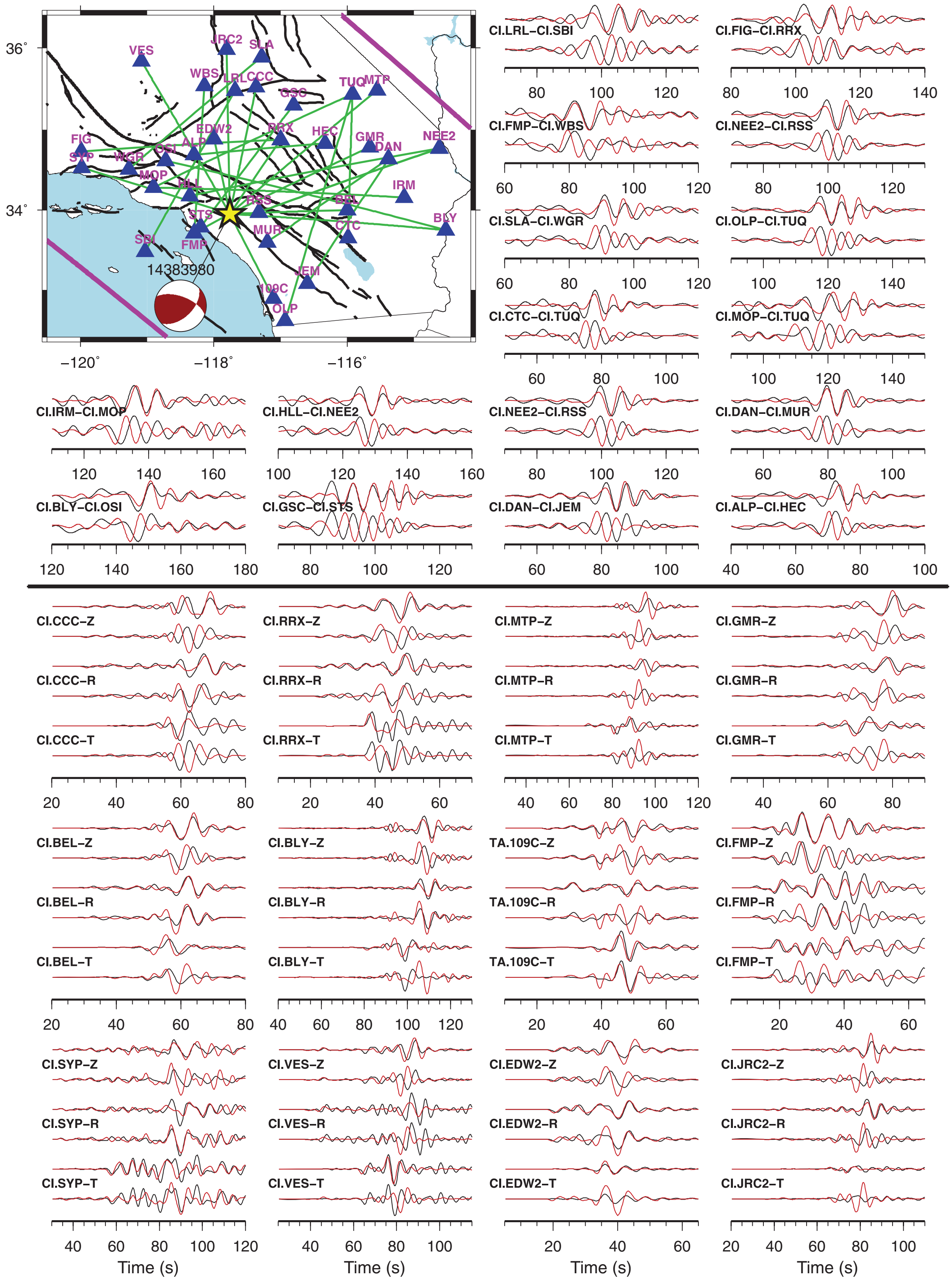

Figure 2. Examples of the observed and synthetic waveform comparisons for CVM4 and CVM4SI2 using the 2008 July 29 M_{w} 5.4 Chino Hills earthquake and some ambient noise Green's functions at different azimuths and different distances. The map shows the epicentre (the star) and the CMT solution (the red beachball) of the Chino Hills earthquake, as well as source-station and interstation paths for the seismograms (the green lines). For waveform comparisons, the black solid lines are observed waveforms from the earthquake and ambient-noise Green's functions and red solid lines are synthetic seismograms calculated for the starting model CVM4 (the red lines below) and our current model CVM4SI2 (the red lines above). The ambient noise Green's functions comparisons are above the thick black line and the earthquake waveform comparisons are below the thick black line.

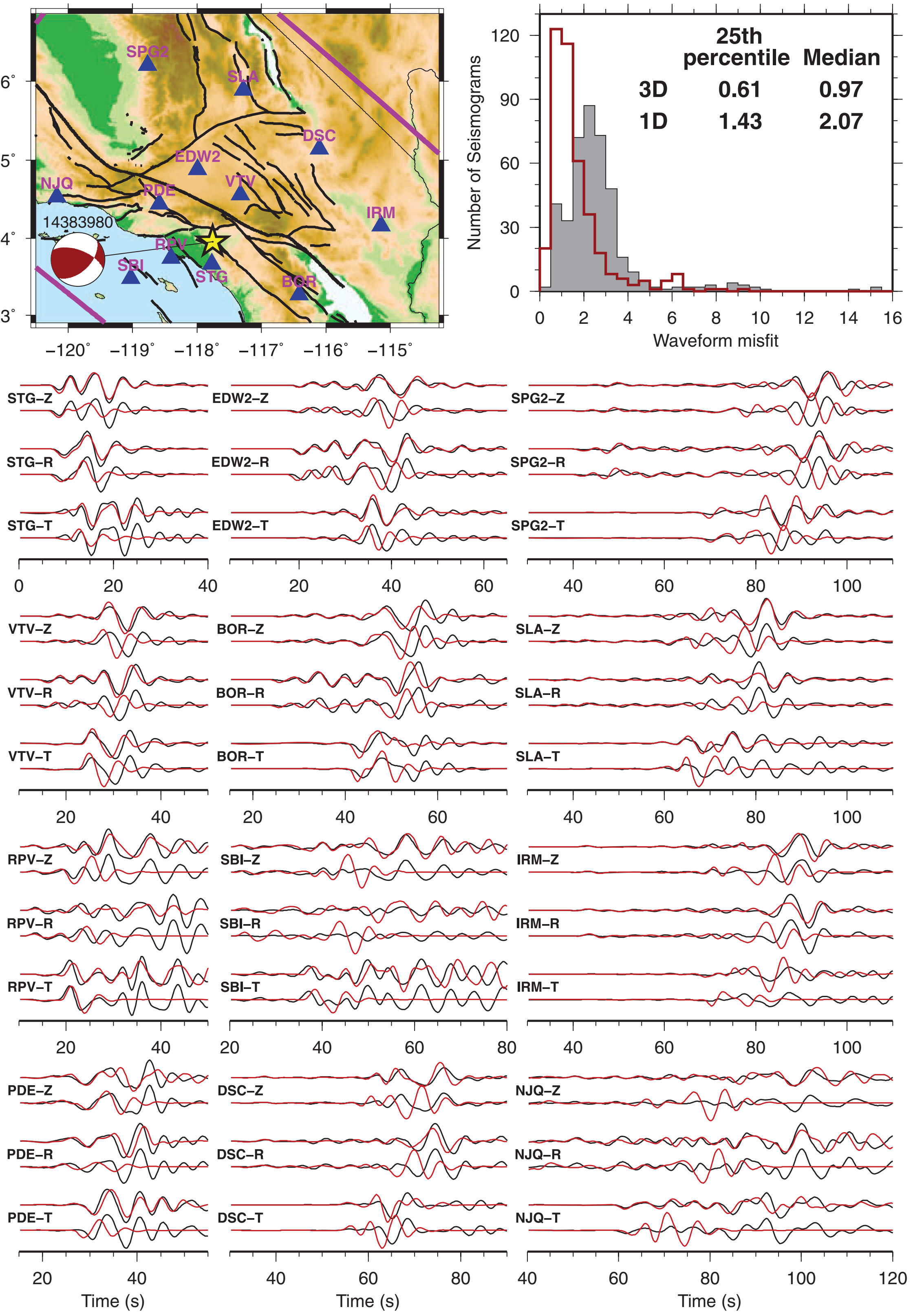

Figure 3. Waveform comparisons for the 2008 July 29 M_w 5.4 Chino Hills earthquake. The histograms show the distributions of waveform misfits for the SoCaL model (grey area) and for CVM4SI2 (area under the red line). Waveform misfits were computed for 414 high-quality seismograms (i.e. signal-to-noise-ratio higher than 10) from 153 stations using eq. (42). The beachball shows the focal mechanism used for computing the synthetics. Example observed and synthetic seismograms for 12 stations (blue triangles) around the epicentre (yellow star) are shown. For the waveform comparison plots, black solid lines are observed seismograms and red solid lines are synthetic seismograms calculated for either SoCaL or CVM4SI2 using the finite-difference code. In each pair of seismograms, the red line above is synthetic seismogram computed using CVM4SI2 and the red line below is the one computed using SoCaL.

recorded by SCSN and its source-station paths provide good sampling throughout the structure model. Our CMT solution for this earthquake is almost identical to the one provided by SCSN moment tensor catalogue. Synthetic seismograms were calculated using the 3-D CVM4SI2 and a slightly modified version of the laterally homogeneous 1-D Standard Southern California Crustal Model (SoCaL; Hadley & Kanamori 1977; Dreger & Helmerger 1993), which was used in Clinton *et al.* (2006) to compute synthetic Green's functions for CMT inversions. In general, the CVM4SI2 synthetics provide much better fit to the observed waveforms than SoCaL synthetics (Fig. 3). The reduction in waveform misfit, which is quantified using eq. (42) below, for 414 four-minute-long seismograms from 153 stations is about 56 per cent. A systematic comparison between CVM3, which is an earlier version of the 3-D SCEC CVM, and SoCaL by using about 2000 seismograms from 67 earthquakes in the Los Angeles region was presented in Chen *et al.* (2007). Waveform misfit, which was quantified using frequency-dependent phase-delay and amplitude anomalies, reduced more than 57 per cent for CVM3 synthetics relative to SoCaL synthetics. Based on the waveform data we have analysed so far, we believe that in general synthetics computed using the 3-D CVM4SI2 provide substantially better fit to the observed waveform data than synthetics computed from the laterally homogeneous SoCaL model in the region of our study (Fig. 1).

4 INVERSION PROCEDURE

We illustrate our inversion procedure using the 2002 September 3 M_{w} 4.3 Yorba Linda earthquake as an example. The epicentre, the best-fitting double couple and the complete CMT solutions for this earthquake are shown in Fig. 4(a).

We retrieve broad-band, three-component seismic waveform data from the Southern California Earthquake Data Center. Two criteria were used to reject seismograms with low SNR,

$$\mathrm{SNR}_A = A_S/A_N, \tag{40}$$

where A_N and A_S are the maximum amplitudes before and after the first-arrival time, and

$$\mathrm{SNR}_E = E_S/E_N = \int_{t_S^0}^{t_S^1} \bar{u}^2(t)dt/(t_S^1 - t_S^0) \bigg/ \int_{t_N^0}^{t_N^1} \bar{u}^2(t)dt/(t_N^1 - t_N^0), \tag{41}$$

where $\bar{u}(t)$ is the observed seismogram, $[t_N^0, t_N^1]$ and $[t_S^0, t_S^1]$ are time windows before and after the first-arrival time. In this study, we rejected seismograms with SNR_A or SNR_E below five. The two horizontal components were rotated into radial and transverse components. We then remove the mean and any linear trend in the seismogram and apply a sixth-order low-pass Butterworth filter with corner frequency at 0.2 Hz. For the 165 earthquakes analysed in this study, the number of seismograms with acceptable SNR ranges from 20 for an M_{L} 3.16 earthquake to 460 for the M_{w} 5.4 Chino Hills earthquake. In general, earthquakes with larger magnitudes usually have more high-quality data seismograms.

The filtered seismogram was then processed using an automated waveform segmentation algorithm to extract waveforms of our interest. Examples of the selected waveforms for the Yorba Linda earthquake are shown in Fig. 4(b). For the CMT inversions in this study, we primarily extracted and fitted the first-arriving *P*- and *S*-waves and the surface waves on the observed seismograms. Our waveform segmentation and selection algorithm is based on the continuous wavelet transform, which allows us to detect and separate different wave groups with intersecting temporal and/or frequency supports. The segmented seismograms are processed using an artificial neural network that is embedded with human knowledge about characteristics of certain seismic wave arrivals to automatically select a set of waveforms of our interest. The same algorithm is also being used in our tomographic inversions. The details of our waveform segmentation and selection algorithm are documented in a separate paper (Diersen *et al.* 2011).

The grid search as formulated in Section 2.2 is then carried out using the selected data waveforms. Throughout the three grid-search stages, the source-model sample space is successively refined around the optimal solutions obtained from the previous stage. The sampling interval reduces from 30° grid-spacing in strike, dip, rake and 2-km spacing in hypocentre locations in the first stage to 5° grid-spacing in strike, dip, rake and 0.5-km spacing in hypocentre locations in the last stage. The source-model subspace selected for refinement is controlled by $\bar{P}_1$ and $\bar{P}_2$ as defined in eqs (19) and (27). In our procedure, we found in general that $\bar{P}_1 = 0.7$ and $\bar{P}_2 = 0.8$ provide a good balance between search efficiency and solution accuracy. Throughout the grid-search step, thresholds $\bar{Q}_0$, $\bar{Q}_1$ and $\bar{Q}_2$, as defined in eqs (17), (25) and (34), are used to reject problematic data waveforms. If the probability for an individual measurement is below the threshold, it suggests that the particular data waveform cannot be fit well by any source solutions in the model sample space, which may due to instrumental problems or unusually high noise level. In our procedure, we found that a value of 0.2 for these three thresholds provide a good balance between solution accuracy and algorithm robustness. The posterior probability density after the third grid-search stage is a 6-D function. The marginal probability densities for strike, dip, rake and depth are plotted in Fig. 4(c).

The optimal solution obtained from the grid-search step is used as the initial solution in an iterative Gauss–Newton optimization as formulated in Section 2.3 and in Zhao *et al.* (2006) to find the optimal coefficients for the six basis moment tensors a_m ($m = 1, 2, \ldots 6$). The partial derivatives of the GSDF measurements with respect to a_m are computed using eqs (38) and (39) and the Gauss–Newton normal equation is solved using the LSQR method (Paige & Saunders 1982). The perturbation obtained in the Gauss–Newton optimization step is quite small, which is due to the fact that the grid search has been carried out through successively refined sample space. The isotropic component of the complete moment tensor is constrained to be zero by setting $a_6 = 0$ in our inversion. For the deviatoric part, we measure the contribution of the non-double-couple component using the parameter $\varepsilon = -\lambda_2/\max(|\lambda_1|, |\lambda_3|)$, λ_1, λ_2 and λ_3 being the eigenvalues of the moment tensor with $\lambda_1 \geq \lambda_2 \geq \lambda_3$ (eq. 1 in Giardini 1983). For the Yorba Linda earthquake ε is less than 4 per cent and the best-fitting

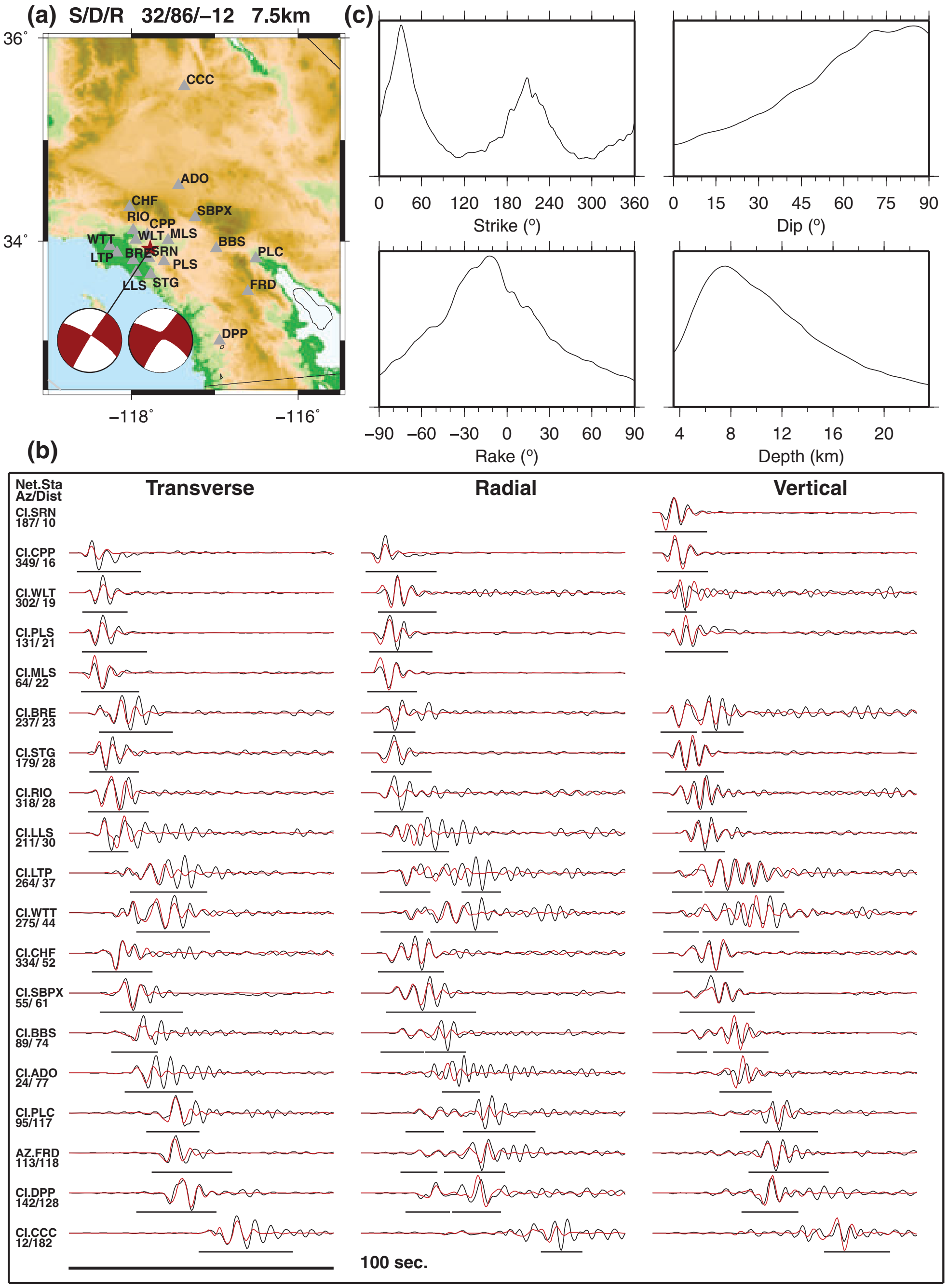

Figure 4. An example of our CMT inversion procedure. (a) The map shows epicentre of the 2002 September 3 M_{w} 4.3 Yorba Linda earthquake (the star) and the best-fitting double couple solution (left beachball) and the full moment tensor solution (right beachball). Stations that have waveforms being selected for our inversion are shown as grey triangles. (b) Examples of the waveforms selected for our CMT inversion using our automated seismogram segmentation and selection algorithm. The black lines are observed seismograms and the red lines are synthetic seismograms computed using our optimal best-fitting double couple solution. The black bars below the seismograms indicate the waveforms we have selected for CMT inversion. (c) The marginal probability densities for strike, dip, rake and depth obtained after our grid-search step.

double couple solution is plotted in Fig. 4(a). In general, for the 165 earthquakes analysed in this study, the value of ε is less than 10 per cent and the best-fitting double couple solutions are shown in the figures.

Depending on the total number of data waveforms used in the inversion, it takes from around 30 s to about few minutes to complete the three stages of grid search on 128 computing cores of the Intrepid (IBM Blue Gene/P) supercomputer at the Argonne Leadership Computing Facility (ALCF). The computational cost for the Gauss–Newton optimization step is negligible compared with that for the grid-search step and it usually takes one computing core less than 5 s for the LSQR algorithm to converge. The disk storage cost is substantial. The RGTs for the 219 stations used in our CMT inversion and also in our full –3-D, full-wave tomographic inversion for Southern California currently occupies around 400 TB (1 TB = 1024 GB) disk space on Intrepid.

5 RESULTS

The SCSN automatically generate and catalogue moment tensor solutions and moment magnitudes for regional earthquakes with local magnitude $M_{\mathrm{L}} > 3.0$ (Clinton *et al.* 2006). This automated algorithm inverts three-component, broad-band waveforms with period from 10 s to 100 s from at least four stations using pre-determined Green's functions for various 1-D seismic velocity profiles calibrated for different regions in Southern California. It can provide reliable moment tensor solutions for local events with $M_{\mathrm{L}} > 4.0$.

We have successfully applied our automated CMT inversion algorithm to 165 earthquakes with local magnitude $3.0 \le M_{\mathrm{L}} \le 5.7$ in Southern California. In general our CMT solutions are consistent with the SCSN automatically generated solutions and our solutions provide better or equally good fit to the observed waveforms for frequencies up to 0.2 Hz. A comparison between the focal mechanisms we have determined with those from the SCSN moment tensor catalogue is shown in Fig. 1. Finite-difference synthetic seismograms were computed using SCSN moment tensor solutions and our own CMT solutions in the same 3-D earth structure model, CVM4SI2. To quantify waveform misfits within a certain time window $[t_0, t_1]$, we use the following normalized misfit measure

$$F = \int_{t_0}^{t_1} dt\, [\bar{u}(t) - u(t)]^2 \Bigg/ \sqrt{\int_{t_0}^{t_1} dt\, [\bar{u}(t)]^2 \int_{t_0}^{t_1} dt\, [u(t)]^2}, \tag{42}$$

where $\bar{u}(t)$ is the observed seismogram and $u(t)$ is the corresponding synthetic seismogram (Zhu & Helmberger 1996). The advantage of this misfit definition is that it prevents a few strongest waveforms from dominating the misfit measure. The P_{nl} waves usually have smaller amplitudes than surface waves and stations close to the source usually have larger amplitudes. The normalization in eq. (42) helps to weight waveforms with different amplitudes equally. We note that this misfit measure is only used for evaluating CMT solutions and it is not used in our inversion algorithm. Waveform misfits are quantified using normalized cross-correlation coefficients, cross-correlation traveltime shifts and amplitude anomalies in our grid-search step and using frequency-dependent GSDF measurements in our Gauss–Newton optimization step. The justifications for not using eq. (42) in our CMT inversion algorithm are discussed in more detail in Section 6.

For the 165 earthquakes analysed in this study, the accumulative waveform misfit (i.e. the summation of F for all selected waveforms and all earthquakes) between the observed seismograms and the synthetics computed using our own CMT solutions is about 86 per cent of the accumulative waveform misfit between observed seismograms and the synthetics computed using SCSN moment tensors. In this comparison, the synthetic seismograms for our own CMT solutions and for SCSN solutions are both computed using CVM4SI2 and the finite-difference method. We note that the forward modelling apparatus used for the comparison is identical to the one used in our CMT inversion, therefore it could produce comparison results favouring our CMT solutions. Ideally, such a comparison should be carried out using an independent forward modelling apparatus with the true earth structure model, which is difficult, if possible at all, in practice. However, we think that in general the 3-D CVM4SI2 provides better predictions of observed waveforms than the laterally homogeneous SoCaL model (e.g. Fig. 3) and might be closer to the actual structure model in general. At the current stage, CVM4SI2 is still being refined through our full-wave tomographic inversions. A more objective comparison could be conducted using an improved version of our tomographically refined 3-D earth structure model, which will be documented in a future publication.

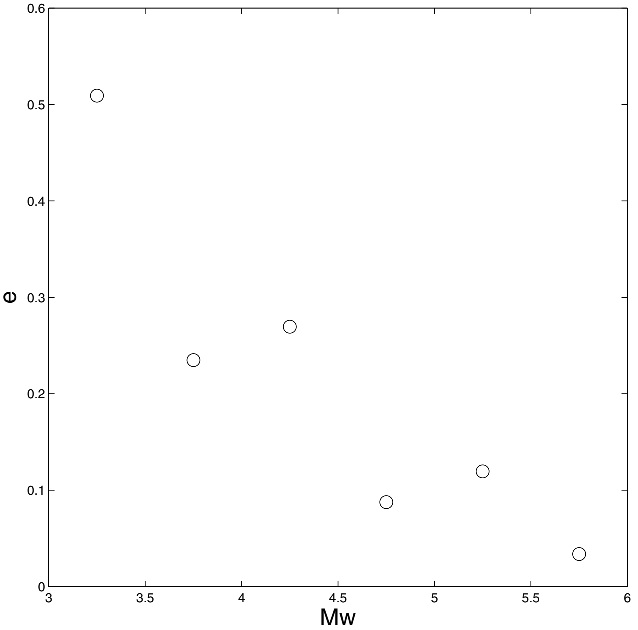

Figure 5. The difference in the normalized moment tensor e (eq. 43) as a function of earthquake moment magnitude. The magnitude interval from 3.0 to 6.0 is separated evenly into six bins. The median of e for earthquakes in each bin is plotted at the centre of each magnitude bin. The peak between magnitude interval from 4.0 to 4.5 may be due to the fact that a number of earthquakes close to the north of Mexico have larger e (Fig. 7).

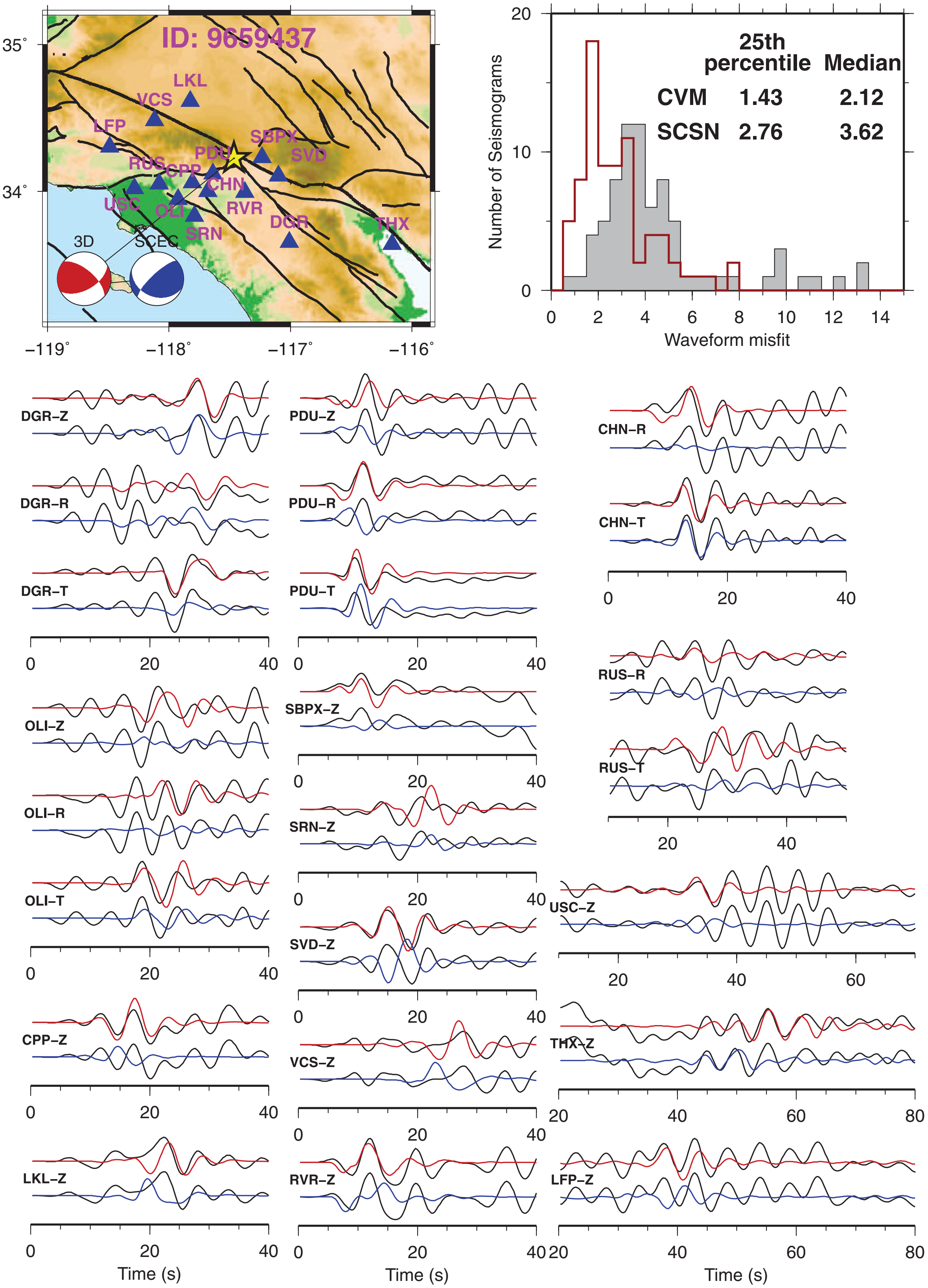

Figure 6. Waveform comparison for a small earthquake used in our study. Red beachball, focal mechanism determined using our CMT inversion algorithm; blue beachball, SCSN focal mechanism. Star, epicentre of the earthquake; blue triangles, station locations of waveform comparison examples. Black solid lines, observed seismograms; red solid lines, synthetic seismograms computed using our optimal CMT solution; blue solid lines, synthetic seismograms computed using SCSN CMT solution. In the box, the histograms show the distributions of waveform misfits of SCSN CMT solution (grey area) and our optimal solution (area included by red line).

Among the 165 earthquakes we have studied, a few of them have larger discrepancies with the SCSN moment tensor solutions. In general, the discrepancies are larger for smaller earthquakes and for earthquakes located close to the boundary of the seismic network. We give a more detailed explanation in the following.

5.1 CMT solutions for small earthquakes

As shown in Fig. 1, for the 165 earthquakes we have analysed so far, the CMT solutions determined using our method are generally consistent with the SCSN solutions. To quantify the differences between our focal mechanisms and SCSN solutions, we define the quantity

$$e = (\hat{\mathbf{M}}_{\mathrm{cvm}} - \hat{\mathbf{M}}_{\mathrm{scsn}}) : (\hat{\mathbf{M}}_{\mathrm{cvm}} - \hat{\mathbf{M}}_{\mathrm{scsn}}), \tag{43}$$

where $\hat{\mathbf{M}}_{\mathrm{cvm}}$ and $\hat{\mathbf{M}}_{\mathrm{scsn}}$ are normalized moment tensors for our focal mechanism and for the SCSN solution. We separate the magnitude range into six bins with 0.5 magnitude interval. The median of e for earthquakes in each bin is shown in Fig. 5. In general, the difference in focal mechanism between our solution and the SCSN solution is larger at smaller magnitudes.

The smallest earthquake we have analysed so far has local magnitude $M_{\mathrm{L}} = 3.16$ (SCSN event ID 9659437). For this small earthquake, the SCSN automatic algorithm inverted waveforms at four stations and its solution is shown in Fig. 6. Due to the small magnitude of this earthquake, the signal-to-noise ratio of observed waveforms with period longer than 10 s is quite low, which partly explains the low variance reduction (7.52 per cent) obtained by the SCSN algorithm. To improve the signal-to-noise ratio of the observed waveforms, we need to reduce the shortest period to below 10 s. The 3-D seismic velocity model CVM4SI2 used in our algorithm can provide accurate Green's functions for frequencies up to 0.2 Hz, which allows us to fit observed waveforms at 5 s or longer. For this small earthquake, the centroid location determined using our algorithm is about 3 km shallower than the SCSN solution and the difference in dip is about 20° (Fig. 6). Comparison with the observed waveforms low-pass filtered to 0.2 Hz shows that the synthetics generated using our CMT solution provide better fit than those generated using the SCSN solution (Fig. 6). We note that the improvements in the waveform fits are caused by differences in the source parameters only. The structure model and the forward modelling apparatus for computing synthetics are identical. For this earthquake, the shallower centroid location in our CMT solution causes different excitations of surface waves, which may explain the better fits to the observed surface waves.

For the 10 smallest earthquakes ($3.11 \le M_{\mathrm{w}} \le 3.51$) analysed in this study, the ratio between the accumulative misfit for our solution and the accumulative misfit for SCSN solution ranges from around 0.44 to around 0.95, which suggests that our solutions fit observed waveforms better than SCSN solutions or equally well in general. By using a well-calibrated 3-D seismic structure model to generate Green's functions, our synthetics can fit observed waveforms at higher frequencies than synthetics generated using 1-D models, thereby providing more robust CMT solutions for earthquakes with smaller magnitudes.

5.2 Effects of station azimuthal coverage

Among the earthquakes with relatively large discrepancies between our CMT solutions and the SCSN solutions, many of them lie close to the boundary of the seismic network (Fig. 7), in which case the station azimuthal coverage can be poor. An example is shown in Fig. 8. For this M_{L} 4.33 earthquake (SCSN event ID 14178236), the difference in centroid location between our solution and the SCSN solution is less than 1 km, the difference in focal mechanism is significant (Fig. 8). Synthetics generated using our CMT solution generally provide better fit to the observed waveforms, especially for longer source-station paths that traverse basins (Fig. 8). The 1-D seismic structure model used for determining the SCSN solution might not provide good approximations for those source-station paths, which introduces a bias into the estimated CMT solution. Such a bias due to inaccuracy in seismic structure model is alleviated when the azimuthal coverage of the seismic stations is good.

5.3 Depths of earthquakes

The RGT database and the reciprocity principle allow us to conduct efficient grid search to find the optimal epicentre locations and depths of earthquakes without running additional wave-propagation simulations. The grid spacing of our RGT database is 500 m, which gives us a spatial resolution up to 250 m in earthquake depth during the grid-search step.

For the 165 earthquakes analysed in this study, their depths range from around 2 km to about 18 km. The amplitudes of the surface waves used in the inversion give us strong constraints on earthquake depths. A comparison of the earthquake depths determined using our own algorithm and those determined by Lin *et al.* (2007a) using a 3-D seismic structure model (Lin *et al.* 2007b) and those extracted from the SCSN moment tensor catalogue is shown in Fig. 9. In general, the depths determined using our own algorithm correlates well with those determined by Lin *et al.* (2007a). For the outliers in Fig. 9(a), we conducted a grid search at the earthquake locations provided by Lin *et al.* (2007a) and generated synthetic seismograms for the optimal focal mechanisms. We found that in general, synthetics generated using our CMT solutions provide better fit to surface-wave amplitudes than those generated using the optimal focal mechanisms at the locations provided by Lin *et al.* (2007a). An example is shown in Fig. 10 for a magnitude about 4.98 earthquake (SCSN event ID 14065544) in the offshore region. For this earthquake, the depth provided by Lin *et al.* (2007a) is 33.97 km and the depth provided by our algorithm is about 13.5 km. Synthetics computed using our CMT solution provide much better fit to the observed waveforms, especially for the surfaces waves.

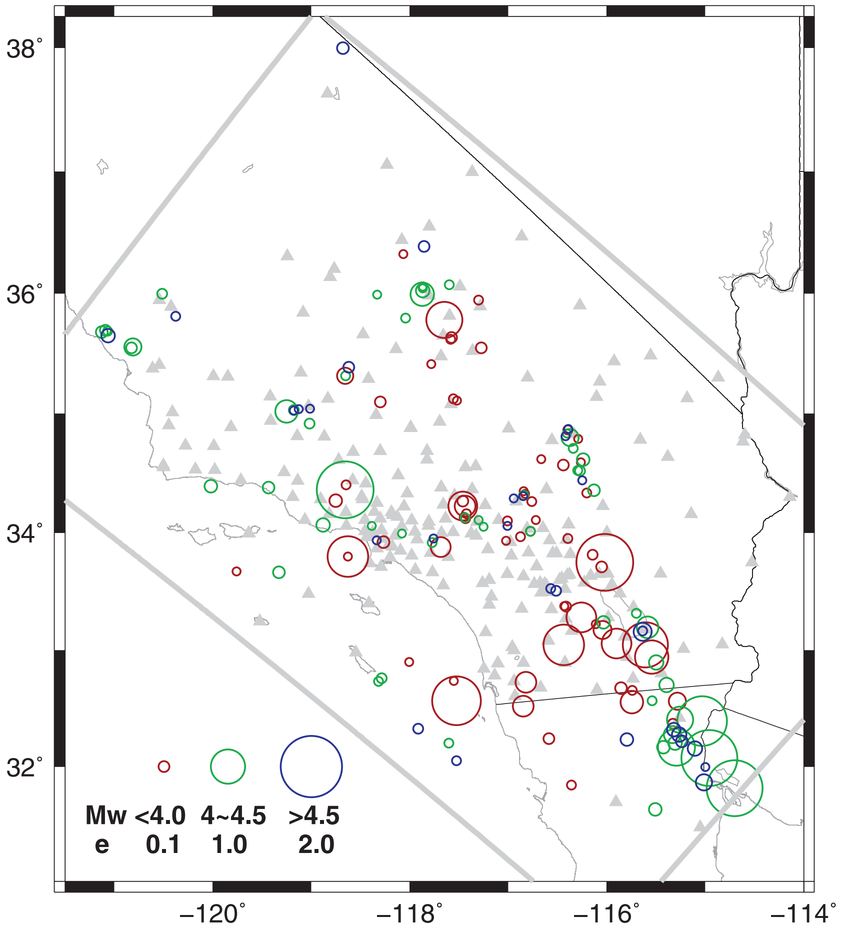

Figure 7. Geographic distribution of the difference in normalized moment tensor *e* (eq. 43). The radii of the circles are proportional to the size of *e* and the centres of the circles are located at the epicentre locations of the analysed earthquakes. The colour of the circle is corresponding to the moment magnitude range of the earthquake.

Synthetics generated using the location provided by Lin *et al.* (2007a) generally do not have sufficient amplitudes for the surface waves, which suggests that Lin *et al.* (2007a) may have overestimated the depth of this earthquake.

5.4 Moment magnitudes of earthquakes

For most of the earthquakes analysed in this study, the moment magnitudes provided by our algorithm are in good agreement with those provided by the SCSN moment tensor catalogue, except for a few outliers (Fig. 11a). The same outliers also exist on the correlation plot between the SCSN M_L and SCSN M_w (Fig. 11b). The correlation plot between our M_w estimates and SCSN M_L estimates (Fig. 11c) has larger scattering than that between our M_w estimates and SCSN M_w estimates. However, for the outliers in Fig. 11(a) and (b), our M_w estimates seem to correlate better with the SCSN M_L estimates than the SCSN M_w estimates, which suggests that the SCSN automated algorithm may have overestimated the moment magnitudes of those earthquakes.

6 DISCUSSION

In this study, we have extended the CMT inversion algorithm based on the RGT database introduced in Zhao *et al.* (2006) to include a grid-search step. The formulation presented in this paper allows us not only to obtain an optimal solution but also to quantify uncertainties in the solution. The procedure allows us to iteratively condition the model space by rejecting solutions with low probabilities. At the beginning of step 2 in our grid-search procedure, by selecting appropriate values for the probability threshold $\bar{P}_1$, we can reject solutions that do not provide sufficiently high NCC values, thereby ensuring the accuracy of the cross-correlation traveltime shifts measured in step 2 and the amplitude anomalies measured in step 3. The sample space and the sampling intervals are successively refined only around regions in the model space that have higher probabilities and high accuracy in the solution is achieved with minimal computing time.

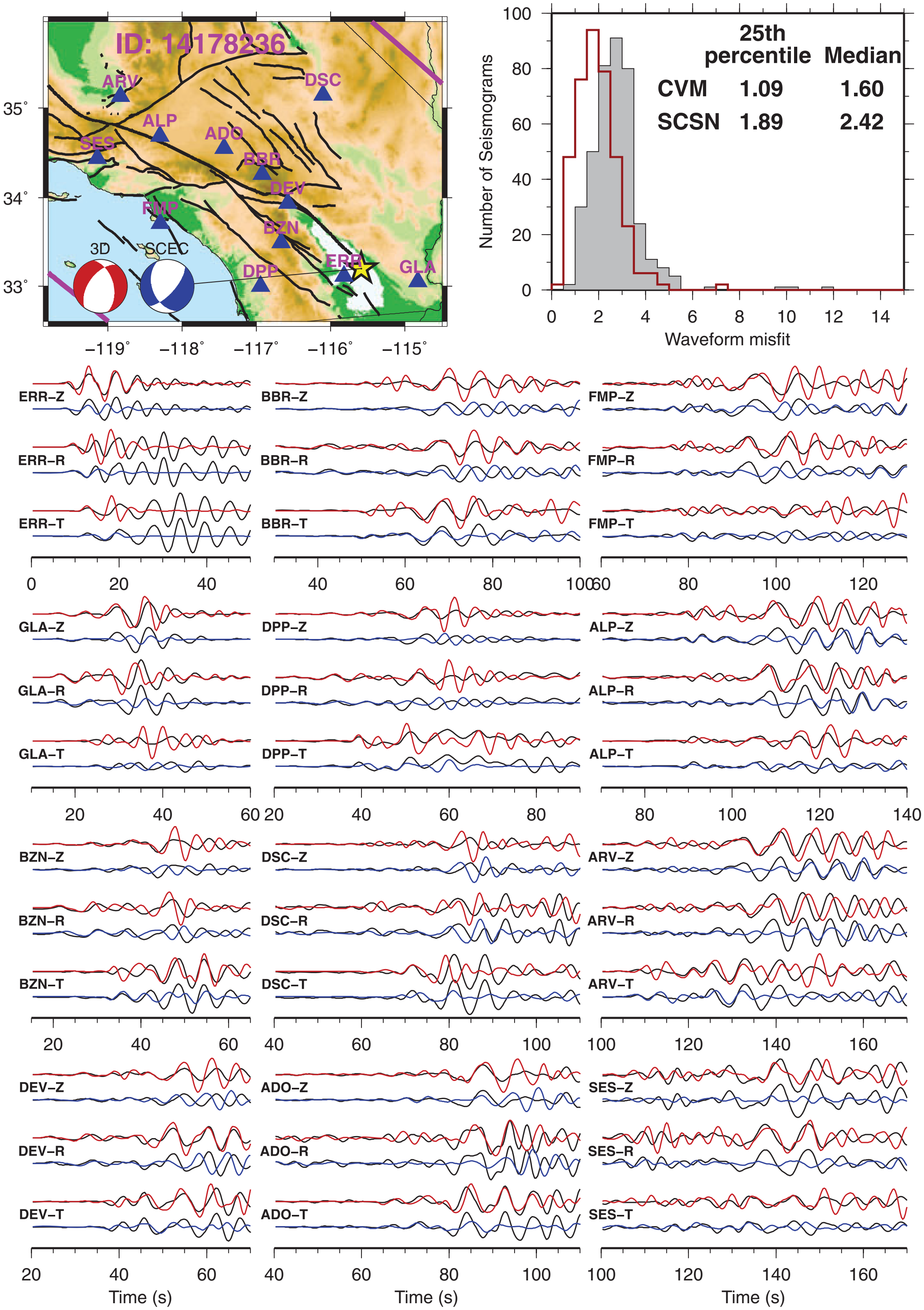

Figure 8. Waveform comparison for an earthquake with relatively poor azimuthal station coverage. Red beachball, focal mechanism determined using our CMT inversion algorithm; blue beachball, SCSN focal mechanism. Star, epicentre of the earthquake; blue triangles, station locations of waveform comparison examples. Black solid lines, observed seismograms; red solid lines, synthetic seismograms computed using our optimal CMT solution; blue solid lines, synthetic seismograms computed using SCSN CMT solution. In the box, the histograms show the distributions of waveform misfits of SCSN CMT solution (grey area) and our optimal solution (area included by red line).

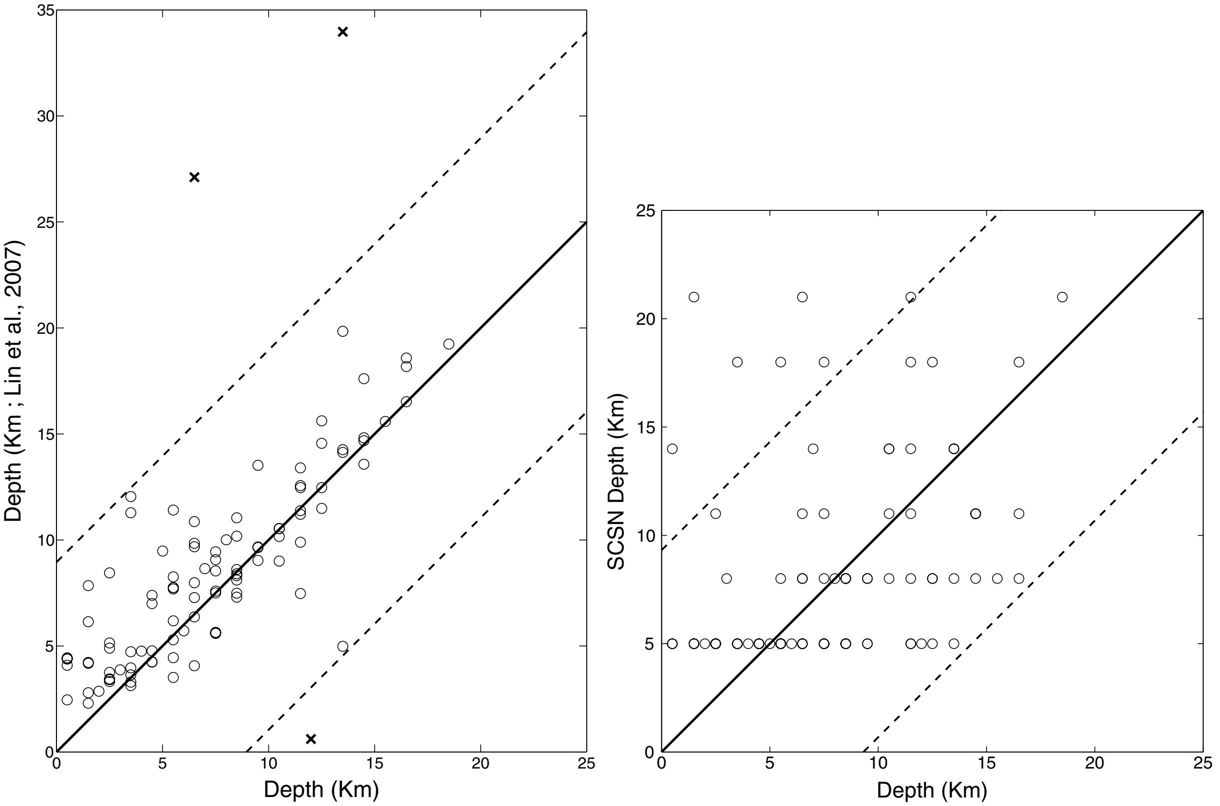

Figure 9. Correlation between earthquake depths determined using our algorithm (horizontal axes) and those determined by Lin *et al.* (2007) (left panel) and those determined by SCSN (right panel). Dash lines indicate locations of two standard deviations. Normal data points are represented as circles and the outliers are represented as crosses.

Unlike conventional waveform-based CMT inversion algorithms that try to minimize waveform differences between synthetic and observed seismograms directly, in this study we have separated the waveform fitting procedure into three steps and used data functionals (i.e. NCC, cross-correlation traveltime shifts and amplitude anomalies) to quantify waveform misfit. In direct waveform-fitting algorithms, amplitude information, which is more sensitive to focal mechanism, is mixed together with phase information, which is affected, to a large extent, by errors in seismic structure models. Such signal-generated noise not only biases the obtained CMT solutions directly, but also makes it more difficult to move to higher frequencies, at which errors in structure models might increase. In this study, we have separated phase information from amplitude information. The cross-correlation traveltime shifts can provide useful constraints on centroid location and centroid time. Their effects on focal mechanism estimates can be controlled through the weighting factor μ_n or by directly constraining the model space.

The CMT inversion algorithm presented in this paper is a generic module of our computational platform for unified seismic data processing and inversion. The observed waveforms selected for CMT inversions are also used in our full –3-D waveform tomography. The RGT database used for generating synthetic seismograms are also used for computing the Fréchet kernels of the GSDF measurements with respect to seismic velocities using the scattering-integral method (Zhao *et al.* 2005). Once a tomographically updated seismic structure model becomes available, the RGT database is re-calculated using the updated structure model and improvements in the structure model is used to obtain better earthquake source models. We expect this unified computational platform will provide seismologists a general tool for seismic waveform analysis and inversion at different geographic scales. In the near future, our computer codes will be freely available to other researchers for non-commercial purposes through the Southern California Earthquake Center (SCEC) Community Modelling Environment (CME) (http://epicenter.usc.edu/cmeportal/index.html).

ACKNOWLEDGMENT

This research used resources of the Argonne Leadership Computing Facility at Argonne National Laboratory, which is supported by the Office of Science of the U.S. Department of Energy under contract DE-AC02–06CH11357. En-Jui Lee is supported by the Southern California Earthquake Center. Po Chen is supported jointly by the School of Energy Resources and the Department of Geology and Geophysics at the University of Wyoming. Comments from two anonymous reviewers improved our manuscript.

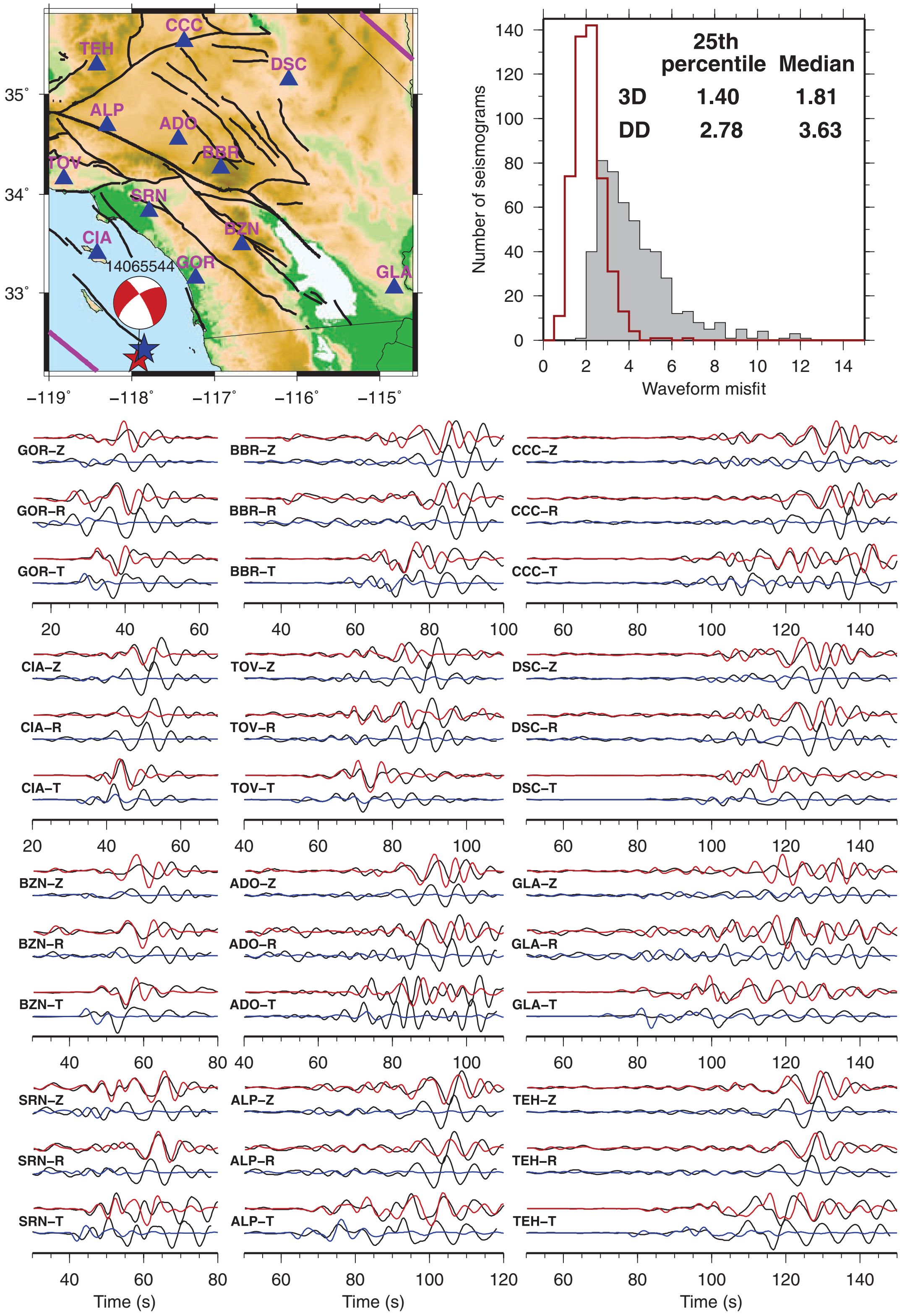

Figure 10. Comparison of waveforms for a magnitude about 4.98 offshore earthquake. Synthetics were generated using the CMT solution determined by our algorithm at our optimal location (red star) and at the location (blue star) provided by Lin *et al.* (2007a). Black solid lines, observed seismograms; red solid lines, synthetic seismograms computed using our optimal CMT solution and location (depth = 13.5 km); blue solid lines, synthetic seismograms computed using our optimal CMT solution at location (depth = 34 km) in Lin *et al.*'s (2007a) catalogue; blue triangles, station locations of waveform comparison examples. In the box, the histograms show the distributions of waveform misfits at Lin *et al.*'s (2007a) location (grey area) and our optimal solution (area included by red line).

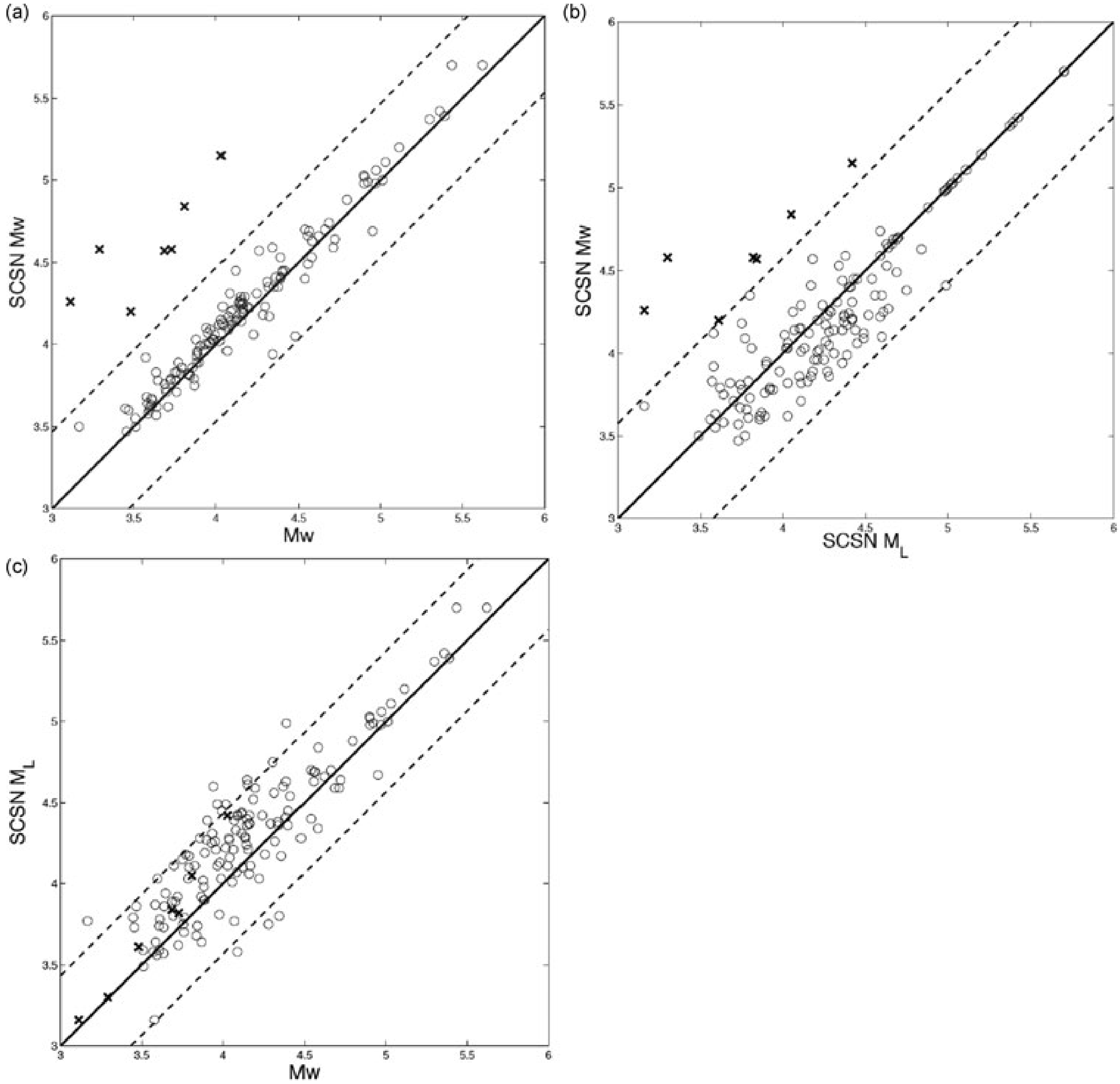

Figure 11. (a) Correlation between the M_{w} determined using our algorithm with the M_{w} determined by SCSN for earthquakes analysed in this study, normal data points are represented as circles and the outliers are represented as crosses; (b) correlation between SCSN M_{w} and SCSN M_{L}; (c) correlation between our M_{w} estimates and SCSN M_{L} for the same set of earthquakes. The dash lines in (a) indicate location of two standard deviations. We note that the same outliers (crosses) in (a) are also plotted as crosses in (b) and (c).

REFERENCES

Akçelik, V. *et al*., 2003. High-resolution forward and inverse earthquake modeling on terascale computers, in *Proceedings of the ACM/IEEE Supercomputing SC'2003 Conference,* Phoenix, AZ.

Aki, K. & Richards, P.G., 2002. *Quantitative Seismology,* 2nd edn, University Science Books, Sausalito, CA.

Chen, P., Zhao, L. & Jordan, T.H., 2007. Full 3D tomography for crustal structure of the Los Angeles region, *Bull. seism. Soc. Am.,* **97,** 1094–1120.

Chen, P., Jordan, T.H. & Lee, E., 2010. Perturbation kernels for generalized seismological data functionals (GSDF), *Geophys. J. Int.,* **183,** 869–883, doi:10.1111/j.1365-246X.2010.04758.x

Clinton, J.F., Hauksson, E. & Solanki, K., 2006. An evaluation of the SCSN moment tensor solutions: robustness of the M_{w} magnitude scale, style of faulting, and automation of the method. *Bull. seism. Soc. Am.,* **96**(5), 1689–1705, doi:10.1785/0120050241.

Diersen, S., Lee, E., Spears, D., Chen, P. & Wang, L., 2011. Classification of seismic windows using artificial neural networks. in *Proceedings of the 11th International Conference on Computer Science,* Tsukuba, Japan.

Dreger, D.S., 2003. TDMT_INV: time domain seismic moment tensor INVersion, in *International Handbook of Earthquake and Engineering Seismology,* Vol. 81B, p. 1627, Academic Press, San Diego, CA.

Dreger, D.S. & Helmberger, D., 1991. Source parameters of the Sierra Madre earthquake from regional and local body waves, *Geophys. Res. Lett.,* **18,** 2015–2018.

Dreger, D.S. & Helmberger, D.V., 1993. Determination of source parameters at regional distances with three-component sparse network data, *J. geophys. Res.,* **98,** 8107–8125.

Dziewonski, A.M., Chou, T.-A. & Woodhouse, J. H., 1981. Determination of earthquake source parameters from waveform data for studies of global and regional seismicity, *J. geophys. Res.* **86,** 2825–2852

Fichtner, A., Kennett, B.L.N., Igel, H., Bunge, H.-P., 2009. Full seismic waveform tomography for upper-mantle structure in the Australasian region using adjoint methods, *Geophys. J. Int.,* **179,** 1703–1725.

Fichtner, A., Kennett, B.L.N., Igel, H., Bunge, H.-P., 2010. Full waveform tomography for radially anisotropic structure: new insights into present and past states of the Australasian upper mantle. *Earth planet. Sci. Lett.,* **290,** 270–280.

Gee, L.S. & Jordan, T.H., 1992. Generalized seismological data functionals, *Geophys. J. Int.,* **111,** 363–390.

Giardini, D., 1983. Regional deviation of earthquake source mechanisms from the 'double-couple' model, in *Earthquakes: Theory and Interpretation,* pp. 345–353, eds. Kanmori, H. & Bosch, E., North-Holland, Amsterdam.

Graves, R., 1996. Simulating seismic wave propagation in 3D elastic media using staggered-grid finite differences, *Bull. seism. Soc. Am.,* **86,** 1091–1106.

Hadley, D. & Kanamori, H., 1977. Seismic structure of the Transverse Ranges, California, *Geol. Soc. Am. Bull.,* **88,** 1469–1478.

Hardebeck, J.L. & Shearer, P.M., 2002. A new method for determining first-motion focal mechanisms, *Bull. seism. Soc. Am.,* **92,** 2264–2276.

Hauksson, E., 2000. Crustal structure and seismicity distribution adjacentvto the Pacific and North America plate boundary in southern California, *J. geophys. Res.,* **105,** 13 875–13 903.

Helmberger, D.V. & Engen, G.R., 1980. Modeling the long-period body waves from shallow earthquakes at regional ranges, *Bull. seism. Soc. Am.,* **70,** 1699–1714.

Hingee, M., Tkalčić, H., Fichtner, A. & Sambridge, M., 2010. Seismic moment tensor inversion using a 3-D structural model: applications for the Australian region. *Geophys. J. Int.,* **184,** 949–964, doi:10.1111/j.1365–246X.2010.04897.x.

Kikuchi, M. & Kanamori, H., 1991. Inversion of complex body waves—III, *Bull. seism. Soc. Am.* **81,** 2335–2350.

Kohler, M.D., Magistrale, H. & Clayton, R.W., 2003. Mantle heterogeneities and the SCEC reference three-dimensional seismic velocity model version 3, *Bull. seism. Soc. Am.,* **93,** 757–774.

Komatitsch, D., Liu, Q., Tromp, J., Süss, P., Stidham, C. & Shaw, J.H., 2004. Simulations of ground motion in the Los Angeles basin based upon spectral-element method, *Bull. seism. Soc. Am.,* **94,** 187– 206.

Lin, G., Shearer, P.M. & Hauksson, E., 2007a. Applying a three-dimensional velocity model, waveform cross correlation, and cluster analysis to locate southern California seismicity from 1981 to 2005, *J. geophys. Res.,* **112,** B12309, doi:10.1029/2007JB004986

Lin, G., Shearer, P.M., Hauksson, E. & Thurber, C.H., 2007b. A three-dimensional crustal seismic velocity model for southern California from a composite event method. *J. geophys. Res.,* **112,** B11306, doi:10.1029/2007JB004977.

Liu, Q.-Y., Polet, J., Komatitcsh, D. & Tromp, J., 2004. Spectral-element moment tensor inversions for earthquakes in Southern California, *Bull. seism. Soc. Am.,* **94,** 1748–1761.

Ma, S., Prieto, G.A. & Beroza, G.C., 2008. Testing community velocity models for southern California using the ambient seismic field, *Bull. seism. Soc. Am.,* **98,** 2694–2714.

Magistrale, H., Day, S., Clayton, R.W. & Graves, R., 2000. The SCEC Southern California reference three-dimensional seismic velocity model Version 2, *Bull. seism. Soc. Am.,* **90,** S65–S76.

Okamoto, T., 1994a. Location of shallow subduction zone earthquake inferred from teleseismic body waveform, *Bull. seism. Soc. Am.,* **84,** 264–268.

Okamoto, T., 1994b. Teleseismic synthetics obtained from 3-D calculations in 2-D media, *Geophys. J. Int.,* **118,** 613–622.

Okamoto, T., 2002. Full waveform moment tensor inversion by reciprocal finite difference Green's function, *Earth Planets Space,* **54,** 715–720.

Olsen, K.B., 1994. Simulation of three-dimensional wave propagation in the Salt Lake Basin, *PhD thesis*. University of Utah, Salt Lake City, 157 pp.

Olsen, K.B., Day, S.M. & Bradley, C.R., 2003. Estimation of Q for long-period (>2 s) waves in the Los Angeles Basin, *Bull. seism. Soc. Am.,* **93,** 627–638.

Paige, C. & Saunders, M., 1982. Algorithm 583 LSQR: sparse linear equations and least squares problems, *ACM Trans. Math. Softw.,* **8**(2), 195–209.

Pasyanos, M.E., Dreger, D.S. & Romanowicz, B., 1996. Towards real-time determination of regional moment tensors, *Bull. seism. Soc. Am.,* **86,** 1255–1269.

Ramos-Martínez, J. & McMechan, G.A., 2001. Source-parameter estimation by full waveform inversion in 3D heterogeneous, viscoelastic, anisotropic media, *Bull. seism. Soc. Am.,* **91,** 276–291.

Ritsema, J., Rivera, L., Komatitsch, D., Tromp, J. & van Heijst, H.J., 2002. The effects of crust and mantle heterogeneity on PP/P and SS/S amplitude ratios, *Geophys. Res. Lett.,* **29,** doi:10.1029/2001GL013831.

Romanowicz, B., Dreger, D., Pasyanos, M. & Uhrhammer, R., 1993. Monitoring of strain release in central and northern California using broadband data, *Geophys. Res. Lett.,* **20,** 1643–1646.

Shearer, P., Hauksson, E. & Lin, G., 2005. Southern California hypocenter relocation with waveform cross-correlation, Part 2: results using source-specific station terms and cluster analysis, *Bull. seism. Soc. Am.,* **95,** 904–915, doi:10.1785/0120040168.

Subramanian, V., Wang, L., Lee, E. & Chen, P., 2010. Rapid processing of synthetic seismograms using Windows azure cloud, in *Proceedings of the IEEE CloudCom 2010*, Indianapolis, IN.

Süss, M.P. & Shaw, J.H., 2003. *P*-wave seismic velocity structure derived from sonic logs and industry reflection data in the Los An- geles basin, California, *J. geophys. Res.,* **108,** 2170, doi:10.1029/2001JB001628.

Thio, H.K. & Kanamori, H., 1995. Moment-tensor inversions for local earthquakes using surface waves recorded at TERRAscope, *Bull. seism. Soc. Am.,* **95,** 1021–1038.

Zhao, L. & Helmberger, D.V., 1994. Source estimation from broadband regional seismograms, *Bull. seism. Soc. Am.,* **84,** 91–104.

Zhao, L., Jordan, T.H., Olsen, K.B. & Chen, P., 2005. Fréchet kernels for imaging regional earth structure based on three-dimensional reference models, *Bull. seism. Soc. Am.,* **95,** 2066–2080.

Zhao, L., Chen, P. & Jordan, T.H., 2006. Strain Green's tensors, reciprocity and their applications to seismic source and structure studies, *Bull. seism. Soc. Am.,* **96**(5), 1753–1763.

Zhu, L. & Helmberger, D.V., 1996. Advancement in source estimation techniques using broadband regional seismograms, *Bull. seism. Soc. Am.,* **86,** 1634–1641.

Zhu, L. & Kanamori, H., 2000. Moho depth variation in Southern California from teleseismic receiver functions, *J. geophys. Res.,* **105**(B2), 2969–2980.